Geophysical Journal International

Geophys. J. Int. (2024) **237,** 217–234
Advance Access publication 2024 January 27
GJI Seismology

https://doi.org/10.1093/gji/ggae042

Artificial age-independent seismic anisotropy, slab thickening and shallowing due to limited resolving power of (an)isotropic tomography

F. Rappisi [1], M. Witek,[2] M. Faccenda [3], A. M. G. Ferreira[4,5] and S.-J. Chang[6]

[1] *Institute of Geophysics and Tectonics, School of Earth and Environment, University of Leeds, Leeds LS2 9JT, United Kingdom. E-mail: francescorappisi@gmail.com*
[2] *Department of Earth and Environmental Sciences, Korea University, Seoul 02841, South Korea*
[3] *Dipartimento di Geoscienze, Università degli Studi di Padova, 35131 Padova, Italy*
[4] *Department of Earth Science, University College London, London WC1E 6BT, United Kingdom*
[5] *CERIS, Instituto Superior Técnico, Universidade de Lisboa, 1049-001 Lisboa, Portugal*
[6] *Department of Geophysics, Kangwon National University, Chuncheon 24341, South Korea*

Accepted 2024 January 25. Received 2023 December 3; in original form 2023 August 10

SUMMARY

Seismic anisotropy is key to constrain mantle flow, but it is challenging to image and interpret it. Existing large-scale tomography models of seismic anisotropy typically show large discrepancies, which can lead to completely distinct geodynamical interpretations. To better quantify the robustness of anisotropy tomography, we create a 2-D ridge-to-slab geodynamic model and compute the associated fabrics. Using the resulting 21 elastic constants, we compute seismic full waveforms, which are inverted for isotropic and radially anisotropic structure. We test the effects of different data coverage and levels of regularization on the resulting images and on their geodynamical interpretation. Within the context of our specific imposed conditions and source–receiver configuration, the retrieved isotropic images exhibit substantial artificial slab thickening and loss of the slab's high-velocity signature below ∼100 km depth. Our results also show that the first-order features of radial anisotropy are well retrieved despite strong azimuthal anisotropy (up to 2.7 per cent) in the input model. On the other hand, regularization and data coverage strongly control the detailed characteristics of the retrieved anisotropy, notably the depth–age dependency of anisotropy, leading to an artificial flat depth–age trend shown in existing anisotropy tomography models. Greater data coverage and additional complementary data types are needed to improve the resolution of (an)isotropic tomography models.

Key words: Numerical modelling; Seismic anisotropy; Seismic tomography; Waveform inversion.

1 INTRODUCTION

Seismic anisotropy is key to infer the state of deformation in the crust and mantle, which in turn is strongly related to the present-day and past flow. Upper-mantle seismic anisotropy, mainly generated by strain-induced lattice/crystal preferred orientation (LPO/CPO) of intrinsically anisotropic minerals (e.g. olivine and pyroxene) is used as a proxy to infer mantle flow (Park & Levin 2002). Radial anisotropy (the difference between the speed between vertically and horizontally polarized shear waves, $\xi = \frac{V_{SH}^2}{V_{SV}^2}$) is the simplest type of anisotropy, which can occur in layered isotropic media with strong contrasts in material properties or any system displaying hexagonal symmetry (Anderson 1961). It can help distinguish between horizontal and vertical mantle flow, and it has helped unravel exciting dynamic processes in the Earth's deep interior (e.g. Chang *et al.* 2015, 2016; Ferreira *et al.* 2019; Chang & Ferreira 2019).

Current global models of shear wave velocity in the whole and upper mantle (e.g., Panning et al. 2010; Ritsema *et al.* 2011; French *et al.* 2013; Schaeffer & Lebedev 2013; Moulik & Ekström 2014; Auer *et al.* 2014; Chang *et al.* 2015) exhibit several common features. Well established observations include high-velocity anomalies corresponding to subducted slabs stagnating at the bottom of the upper mantle or penetrating to the lower mantle, high-velocity anomalies beneath cratons, low-velocity anomalies beneath ridges at ∼100–150 km depth and the age-dependent thickness of the lithosphere and underlying asthenosphere. Nevertheless, there are still substantial inconsistencies between anisotropy tomography models (for a review see, e.g. Chang *et al.* 2014). For example, all

models show positive anomalies of radial anisotropy ($V_{SH} > V_{SV}$) beneath the Pacific oceanic lithosphere, which are associated to first order with horizontal mantle flow as well as a flat depth–age trend in radial anisotropy beneath oceanic plates. However, some 3-D tomography models of radial anisotropy show discrete linear anomalies beneath the Pacific (e.g. S362WMANI, Kustowski *et al.* 2008; SGLOBE-rani, Chang *et al.* 2014), whereas other models show smooth distributions of positive radial anisotropy across the Pacific (e.g. SAVANI, Auer *et al.* 2014; SEMUCB-WM1, French & Romanowicz 2014). Recently, Kendall *et al.* (2021) quantitatively appraised and updated the isotropic and anisotropic upper-mantle structure of SGLOBE-rani beneath the Pacific. They used the spectral element method (SEM) for the forward modelling along with independent seismic data to build the model SPacific-rani, which shows broader linear positive radial anisotropy anomalies than in SGLOBE-rani, but not a single smooth, broad anomaly. Further data and quantitative analysis are needed to continue assessing the robustness of anisotropy tomography.

In this study, we conduct a quantitative, fully integrated seismo-geodynamical analysis to investigate these issues and quantify the robustness of anisotropy tomography and its interpretations. We carry out 2-D mechanical simulations of oceanic plate evolution from ridge to trench and estimate the associated strain-induced anisotropy, building on previous work by Faccenda & Capitanio (2013). We then compute synthetic seismic full waveforms using the SEM of Tromp *et al.* (2008) and the model obtained from the geodynamic simulations and mantle fabric calculations. We subsequently apply the partitioned waveform inversion (PWI) method of Witek *et al.* (2023), which fits waveforms that are assumed to traverse great circle paths from events and stations. This leads to 1-D isotropic shear wave and radial anisotropy profiles simultaneously and then to a 3-D model by combining the estimated 1-D models, attempting to retrieve the input geodynamic model. Some previous studies also used 2-D geodynamical models to interpret the lithospheric structure in seismic tomography images (e.g. Hedjazian *et al.* 2017; Kendall *et al.* 2022). In this study, we go beyond previous work by considering both plate creation (i.e. oceanic ridges) and subduction and, importantly, by performing tomography experiments using synthetic full waveforms with 21 elastic constants computed for the geodynamical model. We test two different receiver distributions, one that we term 'ideal' with receivers evenly and closely distributed over the study area, and one 'realistic' configuration emulating the distribution of seismic stations in the Pacific ocean. We discuss the methodology used in this study in Section 2 and in the Supporting Information. In Sections 3 and 4, we present and discuss the results obtained as well as their implications.

2 METHODS

We model oceanic plate formation, spreading and subduction. We consider a harzburgtic upper mantle and simulate strain-induced LPO development. Seismic waves are propagated through the medium and the resulting three component synthetic waveforms (*S* and *SS* phases as well as multimode surface waves) are then inverted for isotropic and radially anisotropic structure. While recognizing the significance of azimuthal anisotropy in specific geological contexts, our study intentionally omits its inclusion in the inversion process. We focus solely on S-wave velocity and radial anisotropy to meet the primary objectives of this investigation. We acknowledge that this choice may narrow the scope of our findings. Nevertheless, we emphasize that our goal in this work is not to attain the optimal retrieved model, but rather to calculate a model in a conventional manner, mirroring the conditions of typical tomographic studies in oceanic domains. Azimuthal anisotropy, frequently neglected in tomographic studies due to its limited influence on the specific objectives of the investigation and the associated increase in computational complexity, is in line with our deliberate decision. By adhering to this common practice, we aim to ensure the relevance and applicability of our results to a broader range of studies. We recognize the importance of azimuthal anisotropy and plan to address its effect in a separate future study, acknowledging that such investigations can contribute to a more comprehensive understanding of the Earth's interior. A detailed description of the method is given below.

2.1 Geodynamic modelling

Oceanic plate formation, spreading and subsequent subduction are modelled with I2VIS (Gerya & Yuen 2003). The original code has been modified to solve the equations for conservation of mass (eq. 1), momentum (eqs 2–3) and energy (eq. 4) in polar coordinates. In a Lagrangian reference frame and assuming incompressibility these equations take the form:

$$\frac{1}{r}\frac{\partial r v_r}{\partial r} + \frac{1}{r}\frac{\partial v_\phi}{\partial \phi} = 0, \tag{1}$$

$$\phi_{\text{mom}} : \frac{1}{r}\frac{\partial \tau_{\phi\phi}}{\partial \phi} + \frac{1}{r^2}\frac{\partial r^2 \tau_{\phi r}}{\partial r} - \frac{1}{r}\frac{\partial P}{\partial \phi} = 0, \tag{2}$$

$$r_{\text{mom}} : \frac{1}{r}\frac{\partial \tau_{r\phi}}{\partial \phi} - \frac{1}{r^2}\frac{\partial r^2 \tau_{\phi\phi}}{\partial r} - \frac{\partial P}{\partial r} = -\rho g_r, \tag{3}$$

$$\rho C_p \frac{\mathrm{D}T}{\mathrm{D}t} = -\left(\frac{1}{r}\frac{\partial r q_r}{\partial r} + \frac{1}{r^2}\frac{\partial q_\phi}{\partial \phi}\right) + H, \tag{4}$$

where ϕ and r are the tangential and radial coordinates, respectively, $\vec{v}$ is the velocity vector, P is pressure, τ is the deviatoric stress tensor, ρ is density, g_r is the radial gravitational acceleration (9.81 m s^{-2}), C_p is the specific heat capacity, T is the temperature, D/Dt is the Lagrangian time derivative, $\vec{q}$ is the heat flux vector and H is a heat source term accounting for radiogenic, adiabatic and shear heating.

The model domain extends $0^\circ \leq \phi \leq 40^\circ$ in longitude and 700 km in depth, and is discretized using a regular grid with 1001 by 351 nodes. The initial model setup (Fig. 1a) is composed of a left plate defined by an age increasing from 0 to 60 Myr in the $0^\circ \leq \phi \leq 25^\circ$ range, and by a right plate with a constant 20 Myr age. These thermal ages are defined with the half-space cooling model (HSCM, Turcotte & Schubert 2014) for a 90 km thick layer, below which a 0.5 K km^{-1} adiabatic gradient is imposed. The two plates are characterized by a 7 km thick and relatively weak oceanic crust (which lubricates the plates contact at the subduction boundary) and are separated by a $\sim 30^\circ$ dipping weak zone. A 30 km thick sticky-air layer is placed at the top to model the free surface. A plate speed of 4 cm yr^{-1} is applied to the left plate, while the right plate is fixed. The model runs until a mature subduction scenario is established ($\sim$13 Myr; Fig. 1b). Velocity boundary conditions are free slip everywhere, except for the lower permeable boundary where we apply external free-slip (Gerya 2019). The side boundaries are insulating, while a constant $T = 273$ K is used for the sticky-air layer and a $T = 1890$ K is employed for the bottom boundary.

A viscoplastic rheology based on deformation invariants (Ranalli 1995) is used to model the mantle mechanical behaviour. For the oceanic crust we use the Plagioclase An_{75} flow law reported by Ranalli (1995). For the mantle, the effective viscosity is given by

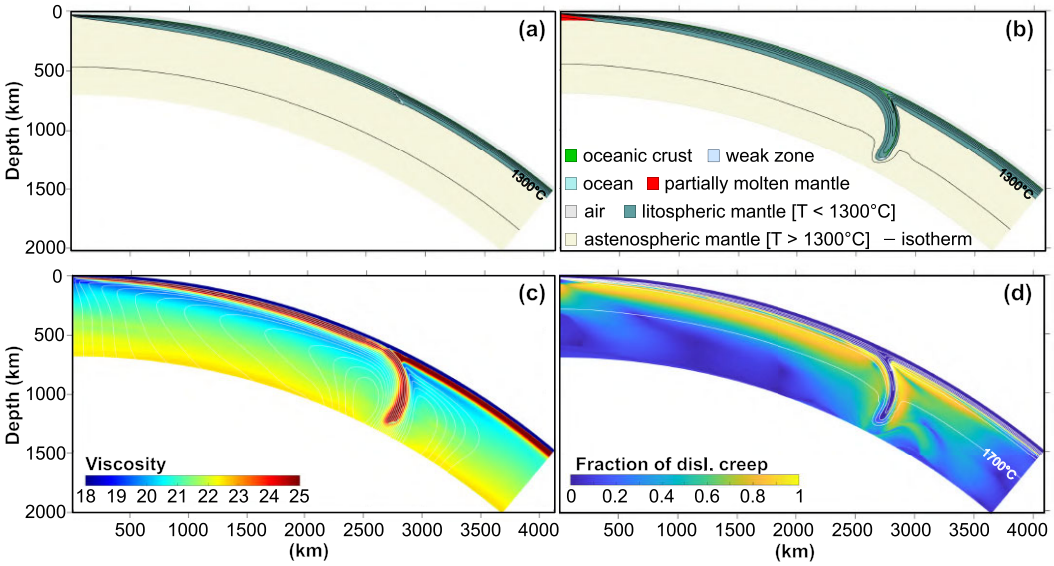

Figure 1. (a) Initial model setup of 2-D oceanic plate formation at the ridge and subsequent subduction. (b) Snapshot at 13 Myr. The black lines are isotherms at every 200 °C. (c) Viscosity exponent (with viscosity in Pa·s) and (d) Fraction of deformation accommodated by dislocation creep at 13 Myr; the white lines are streamlines in (c) and isotherms taken every 200 °C in (d). For further details see Section 2 and Section S1 of the Supporting Information.

the harmonic average of the combined dislocation, diffusion and Peierls creep mechanisms (the corresponding parameters and their physical meaning are given in Table 1),

$$\eta_{\text{ductile}} = \left(\frac{1}{\eta_{\text{disl}}} + \frac{1}{\eta_{\text{diff}}} + \frac{1}{\eta_{\text{peierls}}} \right)^{-1}, \tag{5}$$

where the dislocation and diffusion creep viscosities η_{disl}, η_{diff} are given by Karato & Wu (1993),

$$\eta = \frac{\tau}{2\dot{\varepsilon}}, \tag{6}$$

with the strain rate being given by

$$\dot{\varepsilon} = A \left(\frac{\tau}{\mu} \right)^n \left(\frac{b}{d} \right)^m exp\left(- \frac{E + PV}{RT} \right). \tag{7}$$

Table 1 gives the specific parameter values (pre-exponential factor A, activation energy E, activation volume V, stress exponent n, grain-size exponent m, gas constant R, shear modulus μ, Burgers vector b and grain size d) for the cases of diffusion (η_{diff}) and dislocation creep (η_{disl}), which are analogous to those used by Hedjazian *et al.* (2017).

At high deviatoric stresses (greater than 0.1 GPa) and low-T conditions, creep is accommodated via the Peierls mechanism as given by Katayama & Karato (2008)

$$\eta_{\text{peierls}} = 0.5 A \tau_{\text{II}}^{-1} \exp\left\{ \frac{E + PV}{RT} \left[1 - \left(\frac{\tau_{\text{II}}}{\sigma_{\text{Peierls}}} \right)^p \right]^q \right\}, \tag{8}$$

where τ_{II} is the second invariant of the deviatoric stress tensor and all the other parameters are defined in Table 1. A pseudo-plastic viscosity is also computed as

$$\eta_{\text{pl}} = \frac{\tau_y}{2\dot{\varepsilon}_{\text{II}}}, \tag{9}$$

where $\dot{\varepsilon}_{\text{II}}$ is the second invariant of the strain rate and the plastic strength τ_y is determined with a plastic Drucker–Prager criterion

$$\tau_y = C_{\text{DP}} + \mu P, \tag{10}$$

where $C_{\text{DP}} = C\cos\phi = 1$ MPa is the cohesion, $\mu = \sin\phi$ is the friction coefficient and ϕ is the friction angle. To model strain-induced brittle weakening, the initial friction coefficient is linearly decreased from 0.6 to 0.4 in the $0.5 \leq \varepsilon_p \leq 1.5$ range, where ε_p is the accumulated brittle/plastic strain. For the crust, we use a constant $\mu = 0.05$ to ensure lubrication at the plate's contact. Finally, the effective viscosity is given by

$$\eta_{\text{eff}} = min(\eta_{\text{ductile}}, \eta_{\text{pl}}). \tag{11}$$

The lower and upper cut-off of η_{eff} are set to 10^{18} and 10^{25} Pa·s, respectively. The set of rheological parameters used in this study is similar to that employed in previous numerical studies (e.g. Hedjazian *et al.* 2017; Yang & Faccenda 2020; Lo Bue *et al.* 2021, 2022; Kendall *et al.* 2022), and among other key features it reproduces a 100–120 km thick, low-viscosity asthenospheric channel dominated by dislocation creep (Figs 1c and d).

2.2 LPO development

We consider upper mantle aggregates with olivine:enstatite = 70:30 in volume proportion, mimicking a harzburgitic composition and with a regular 5 km spacing. The development of strain-induced LPO fabrics in the upper mantle aggregates is computed with the modified version of D-Rex (Kaminski *et al.* 2004) included in the software package ECOMAN (https://newtonproject.geoscienze.unipd.it/ecoman). It is regulated by three key parameters—the nucleation (λ), grain-boundary mobility (M) and volume threshold (χ) for activation of grain-boundary sliding—and by the normalized reference dimensionless critical resolved shear stress (nCRSS). The resulting elastic tensor, defined by 21 independent elastic constants, is interpolated to an Eulerian grid with lateral spacing $\Delta\phi = 0.1^\circ$ and with depth spacing $\Delta r = 10$ km. The 2-D grid is then replicated along latitude θ each 0.1° with respect to the equatorial plane in the range between −40° and +40°, and reflected with respect to the ridge axis, so that the final Eulerian domain in (ϕ,r,θ) is 80° × 700 km × 80°. The resulting 3-D computational domain is

Table 1. Creep parameters for mantle rocks.

Property	Symbol	Value	Unit
Diffusion creep (Karato & Wu 1993)			
Pre-exponential factor	A	8.7×10^{15}	s^{-1}
Activation energy	E	300	kJ mol^{-1}
Activation volume	V	6	cm^3 mol^{-1}
Stress exponent	n	1	–
Grain-size exponent	m	2.5	–
Dislocation creep (Karato & Wu 1993)			
Pre-exponential factor	A	3.5×10^{22}	s^{-1}
Activation energy	E	540	kJ mol^{-1}
Activation volume	V	20	$cm^3 mol^{-1}$
Stress exponent	n	3.5	–
Grain-size exponent	m	0	–
Peierls Creep (Katayama & Karato 2008)			
Pre-exponential factor	A	$10^{7.8}$	$Pa^2 s$
Activation energy	E	532	kJ mol^{-1}
Activation volume	V	12	cm^3 mol^{-1}
Peierls stress*	σ_{Peierls}	9.1	GPa
Exponent	p,q	1,2	-,-

Notes. $R = 8.313$ J $mol^{-1}K^{-1}$ is the gas constant, $\mu = 80$ GPa is the shear modulus, $b = 0.5$ nm is the Burgers vector, and $d = 1$ mm is the grain size. * Evans & Goetze (1979).

then characterized by two subduction zones which are symmetric with respect to the central oceanic ridge.

Before computing upper mantle fabrics in the 2-D subduction models, we extensively tested the λ, M, χ and nCRSS parameters on a single aggregate of crystals with either dunitic or harzburgitic composition. These parameters were calibrated and validated by comparison with recent high-strain experimental data and previous studies (e.g. Raleigh *et al.* 1971; Nicolas *et al.* 1973; Kohlstedt & Goetze 1974; Durham & Goetze 1977; Bai *et al.* 1991; Jin *et al.* 1994; Hanson & Spetzler 1994; Zhang & Karato 1995; Warren *et al.* 2008; Faccenda 2014; Hansen *et al.* 2014; Boneh *et al.* 2015; Tasaka *et al.* 2017; Rappisi & Faccenda 2019; Ferreira *et al.* 2019; Sturgeon *et al.* 2019; Lo Bue *et al.* 2021, 2022; Kendall *et al.* 2022). Please, refer to Section S1 and Fig. S1 of Supporting Information for a detailed description of the preliminary numerical experiments. Table S1 in the Supporting Information summarizes the selected parameters.

2.3 Seismological forward modelling

We use SPECFEM3D_GLOBE—based on the SEM (Komatitsch & Tromp 1999; Chen & Tromp 2007; Tromp *et al.* 2008, see Section S2, Supporting Information)—to simulate seismic wave propagation through the medium obtained from the geodynamical simulations and fabric calculations presented in the previous sections, interpolated onto a depth-variable grid (Sadourny 1972; Aki 1980; Ronchi *et al.* 1996; Dahlen & Tromp 2021). From the surface, the cell sizes are doubled at each major discontinuity (i.e. Moho, 670 km and core–mantle boundary), maintaining this coarser resolution until the next discontinuity, where it is doubled again, and this pattern continues down to the bottom of the model (see Fig. 2). The original SPECFEM3D_GLOBE code was modified to incorporate the density and 21 elastic moduli of the geodynamic model in the depth range $24 \leq z \leq 670$ km. Elsewhere, we use Preliminary Reference Earth Model (PREM; Dziewoński & Anderson 1981), and we specify a crustal layer that is characterized by two discontinuities at 14.0 and 24.4 km depth with identical properties as in PREM. Further details on the SEM and the size of the calculation grid are provided in Section S2 of the Supporting Information.

We compute a total of ∼52 080 60-min-long synthetic seismograms recorded by 1302 stations equally spaced 1° apart, from shallow (i.e. ∼10–20 km depth) and deep (i.e. ∼100–600 km depth) events. The initial data set is subsequently reduced by roughly 8 per cent due to quality control measures such as azimuthal amplitudes in the radiation pattern, the signal-to-noise ratio, and arrival times of filtered envelope maximum, which are given in detail in Witek *et al.* (2023). The array of stations is placed above the ridge (at 80°E) and the eastern slab (105°E) extending from 72°E to 113°E and from 15°N to 15°S. We use 40 earthquakes with magnitudes $5 < M_w < 8$ and at local and teleseismic distances with respect to the seismic array. Most of the events are placed in correspondence of the two subduction zones and at the ridge (Fig. 3). The chosen distribution of sources and receivers is designed to simulate two distinctive scenarios: an idealized case and a more realistic setup that closely resembles those commonly employed in similar tomographic studies. The idealized scenario serves as a baseline for comparison, allowing us to evaluate the impact of simplifications and assumptions on our results. In parallel, the more realistic distribution is tailored to mimic the configurations utilized in tomographic investigations, ensuring the relevance and applicability of our findings to real-world scenarios. This dual approach facilitates a comprehensive evaluation of our tomographic results under varying conditions, thereby enhancing the robustness of our study. In Fig. 4, the azimuthal distribution of the ray paths at each gridpoint, separated by vertical and radial component fits (Rayleigh), and transverse component fits (Love). It exhibits only a few regions in the centre of the array that have good azimuthal coverage. Elsewhere, the grid is dominated by a few azimuths. Maps of data coverage—column sums of the weighted coefficients matrix $C_e^{(-1/2)}G$—are shown in Fig. 5. Each column of G corresponds to a model parameter, so a large column sum means that parameter was 'hit' more often. The dark N-S linear feature on the left comes from a waveform fit with anomalously low

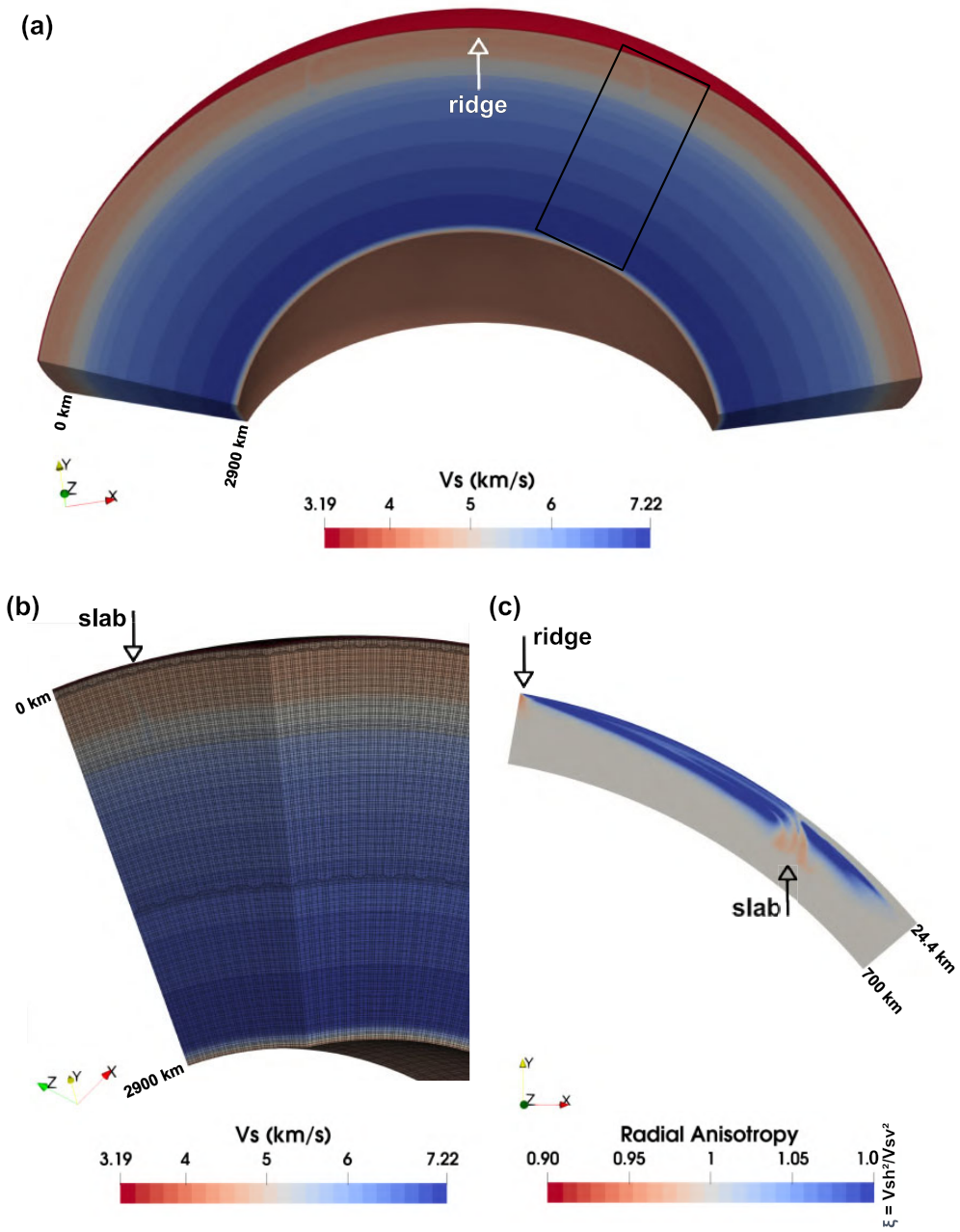

Figure 2. (a) Isotropic shear velocity (V_S) used to perform the seismic forward modelling; (b) zoom of the SPECFEM3D_GLOBE mesh from 0 to 2900 km depth as shown by the black box in (a); and (c) radial anisotropy of the 2-D section that is replicated perpendicular to the ridge axis and reflected with respect to the ridge axis, from 24.4 km (Moho depth) to 670 km.

estimated error—making $C_e^{(-1/2)}$ high. We note that the azimuthal distribution in Fig. 4 is also consistent with the ray paths we can see between 80E-105E.

The minimum accurate wave period is $T_{\min} = \sim 10$ s. For simplicity, attenuation, gravity, ocean, topography and bathymetry effects on seismic wave propagation have been neglected. We use SEM waveforms in Seismic Analysis Code format (SAC; Goldstein & Snoke 2005), which we decimate to 1 Hz. To avoid fitting waves with periods less than $T_{\min}$, we set a maximum fitting frequency of 83 mHz.

2.4 Automated PWI method

In order to test the ability of widely used seismic tomography methods based on ray theory to retrieve the input geodynamic model, the seismic waveforms are inverted for isotropic and radially anisotropic (Love 1927) using an automatic algorithm based on the PWI method (Nolet 1990; Witek *et al.* 2023). A brief description of the method is given as follows. Waveforms are modelled along great circle paths using a local modes approach,

$$u(\omega) = \sum_n A_n(\omega) \exp\left\{ i \int k_n(\omega, s) \mathrm{d}s \right\}, \tag{12}$$

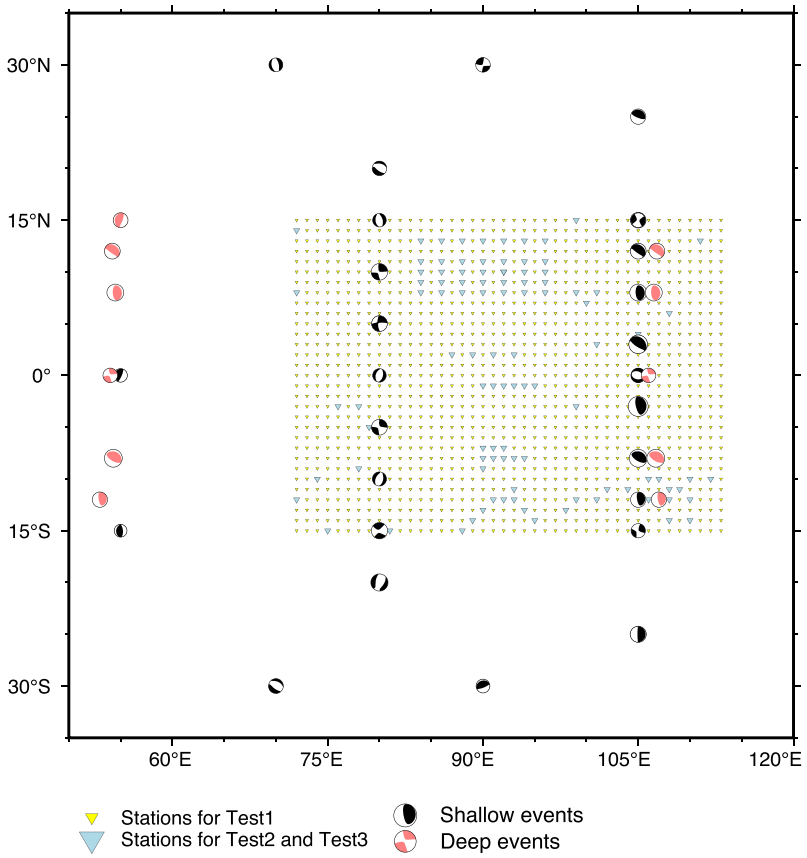

Figure 3. Seismic array with sources (beach balls) and stations (triangles) distribution. Shallow events are in the range between 10 and 20 km depth. Deep events go from 100 to 600 km depth. Events at ∼50°E and ∼105°E are located in correspondence of the two subduction zones. Events at 80°E are located in the oceanic ridge area.

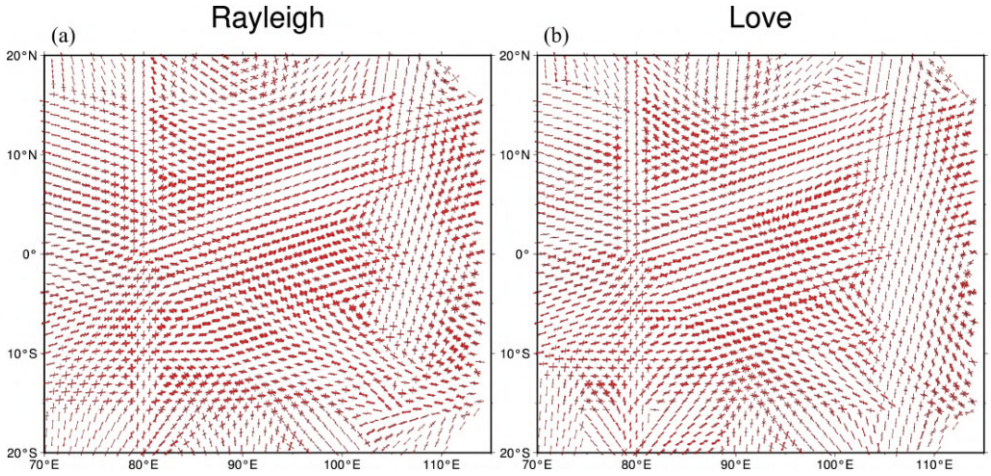

Figure 4. Azimuthal distribution of the ray paths at each gridpoint. Ray paths passing through each cell are plotted symmetrically at the centre of the cell in the style of a rose diagram. The data are separated by (a) vertical and radial component fits—Rayleigh—, and (b) transverse component fits—Love.

where $u(\omega)$ is the displacement response at frequency ω, $A_n(\omega)$ is a complex excitation coefficient for mode n, and $k_n(\omega, s)$ is the local wavenumber for the position s along the great circle arc. The wavenumbers are calculated by solving the normal mode eigenfrequency–eigenfunction problem for a 1-D Earth using a 1-D profile extracted from the 3-D model directly under the position s (Woodhouse 1988; Dahlen & Tromp 2021). More information on the reference 3-D model used in this study is given below. The excitation coefficients $A_n(\omega)$ include source effects and local receiver effects. Since the SEM waveforms used in this study are calculated without the effects of attenuation, attenuation due to Q structure along the ray path is also neglected here. We performed validation

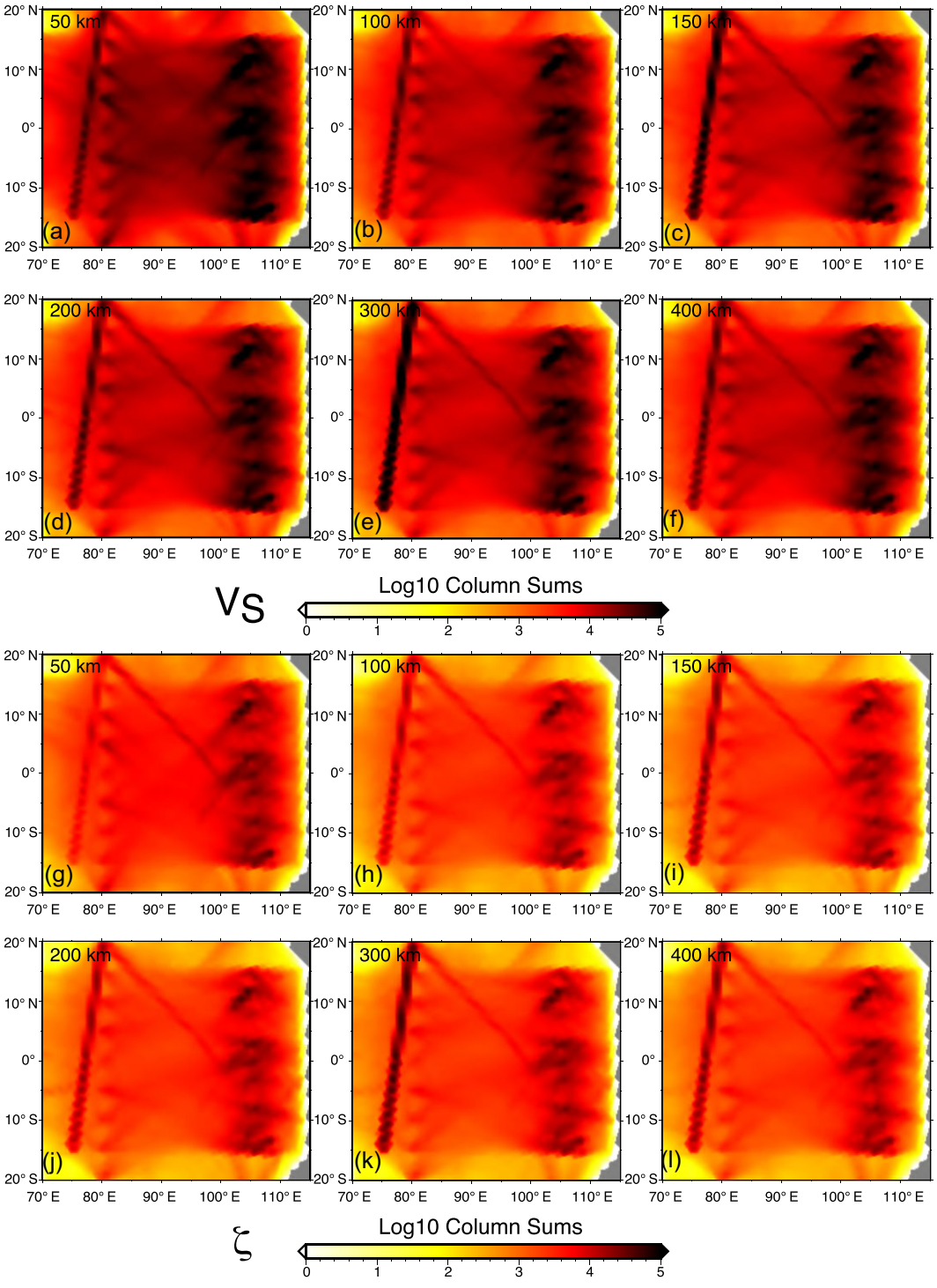

Figure 5. Depth-dependent data coverage for (a)–(f) *S*-wave isotropic velocity and (g)–(l) radial anisotropy. Column sums of the weighted coefficients matrix.

comparisons of waveforms computed using the SEM and the forward modelling scheme used within our automated PWI method for simple 1-D Earth models and found an excellent agreement between the two sets of synthetic seismograms.

Perturbations in the waveforms with respect to the reference 3-D model are assumed to be entirely due to perturbations in the wavenumbers, that is,

$$k_n(\omega, s) = k_n^{ref}(\omega, s)\big(1 + \delta \ln k_n(\omega, s)\big). \tag{13}$$

To first order, the perturbations in the wavenumbers can be related to changes in the local model parameters, $\delta \ln m_i(s, r)$ via sensitivity kernels $K_i(\omega, s, r)$,

$$\delta \ln k_n(\omega, s) = \int_0^a \sum_i K_{ni}(\omega, s, r)\delta \ln m_i(s, r)\mathrm{d}r, \tag{14}$$

where $i = 1, 2, \ldots, 6$ represents different model parameters (*e.g.* ρ, V_P, V_S, ζ_S, ζ_P and η), depending on the parametrization. In PWI, we make the simplifying assumption that the model perturbations

can be represented by a path average that is expanded onto a small set of radial basis functions $h_j(r)$,

$$\overline{\delta \ln m_i}(r) = \frac{1}{\Delta}\int_{\Delta} \delta \ln m_i(s,r)\mathrm{d}s = \sum_j \gamma_{ij} h_j(r), \tag{15}$$

where the γ_{ij} are the basis function coefficients and Δ is the epicentral distance. In this study, we use triangular basis functions, with the first and last basis functions being half-triangles. With these assumptions, the path integral in eq. (12) becomes

$$\int_{\Delta} k_n(\omega, s)\mathrm{d}s = \overline{k_n^{ref}}(\omega)\Delta + \sum_i \sum_j \gamma_{ij}\overline{K_{nij}}(\omega), \tag{16}$$

where $\overline{k_n^{ref}}(\omega)$ is a path average wavenumber calculated through the reference 3-D model and $\overline{K_{nij}}(\omega)$ is a path average sensitivity kernel.

We solve for the γ_{ij} coefficients using a nonlinear waveform fitting algorithm, with the details given in Witek *et al.* (2023). The data fitting is generally split into two parts: (1) fundamental mode extraction and fitting, and (2) full mode sum fitting. In (1), we perform phase-matched filtering to extract the fundamental mode from the observed seismogram (Herrin & Goforth 1977; Goforth & Herrin 1979). After a minimum fitting frequency is determined, the extracted fundamental mode is subjected to a series of Gaussian bandpass filters. We determine window boundaries for each filtered waveform by finding where the envelope drops below one fourth of the maximum value, and we refer to each filtered, windowed waveform as a time–frequency window. In order to minimize the chances that we are fitting unmodelled phases or effects such as scattering, we perform a series of checks on each time–frequency window. We require that the minimum fitting frequency permits at least three fundamental mode wavelengths between the source and receiver to ensure the far-field approximation. The minimum frequency also cannot permit more than 12 wavelengths to avoid cycle skips (Lebedev *et al.* 2005). We avoid fitting waves that are significantly affected by source effects and off-great-circle propagation by checking the fundamental mode source radiation pattern and excluding traces that correspond to nodal directions, and we check that the amplitude ratio between the synthetic and observed waveforms is less than 5.

After fitting the fundamental mode, we use the resulting path average model as an initial model to fit the full synthetic waveform, which contains all modes $n = 0, 1, 2, \ldots, 20$. Summing up to the 20th overtone ensures that the *S*- and *S*-wave multiples can be sufficiently reconstructed, but we note that this does not necessarily imply that all modes will be equally constrained. When fitting the full synthetic, we set an early time limit to be 10 per cent before the predicted *S*-wave arrival if the source–receiver distance is less than 35°. Otherwise, we use the predicted *SS*-wave arrival time. This is done in order to prevent fitting body waves that bottom in the complex lower mantle, since we ignore the 2-D nature of the sensitivity kernels (Marquering & Snieder 1995; Van der Lee & Nolet 1997).

2.5 3-D reference model

The algorithm we use to solve the eigenfrequency–eigenfunction problem for a 1-D Earth model is limited to the case of radial anisotropy (Woodhouse 1988). Therefore, the elastic tensor used in the forward problem is rotated to local spherical coordinates, and we calculate the five Love parameters A, C, N, L and F (Love 1927) via an azimuthal average around the local vertical axis (Montagner & Nataf 1986, 1988). We decompose the elastic tensor into a sum of a purely radially anisotropic elastic tensor and a perturbation that describes the azimuthal anisotropy. Maps showing the calculated 2θ and 4θ variations for fundamental mode Rayleigh and Love wave phase velocities at 80 s period are shown in Fig. 6. The maximum perturbation due to 2θ azimuthal anisotropy is ∼2.7 per cent near the trench for Rayleigh waves at ∼80 s period, with a fast axis orientation perpendicular to the strike of the trench. The maximum perturbation due to 4θ azimuthal anisotropy is ∼ 1.9 per cent also near the trench at ∼ 80 s period for Love waves, with a fast axis orientation of 45°. On the other hand, 4θ variations for Rayleigh waves and 2θ variations for Love waves are less than 0.1 and 0.2 per cent, respectively. That Rayleigh waves are mostly sensitive to 2θ variations, while Love waves are sensitive to 4θ variations is in good agreement with theoretical predictions for realistic mantle structure (Montagner & Nataf 1986, e.g.). In this study, we ignore the effects of azimuthal anisotropy and only consider radial anisotropy for the waveform fitting under the assumption of sufficient azimuthal averaging (Montagner & Nataf 1988). However, we aim to explore the effects of ignoring azimuthal anisotropy in a future study.

A good reference model is necessary to avoid significant artefacts when conducting a linear tomographic inversion (e.g. van der Hilst & Spakman 1989; Nolet 1990; Kissling *et al.* 1994; Van der Lee & Nolet 1997). To that end, we construct a 1-D model for V_{SV} and V_{SH} by laterally averaging the geodynamic model over longitude. Then, we create a 3-D reference model by replacing L and N in the elastic tensor with values from the 1-D model at the appropriate depths. This may be analogous to some studies where a reference 1-D model is first created, after which 3-D perturbations are retrieved in a tomographic inversion (e.g. Kustowski *et al.* 2008). In our case however, since we only solve for shear wave perturbations in our inversion, using a 1-D model for ρ, V_{PV}, V_{PH} and η will make it more difficult to disentangle competing modelling errors. Therefore, in this study our reference model only uses a regional 1-D model average for V_{SV} and V_{SH}, while the other model parameters are left identical to true 3-D variations in the geodynamic model. The effects of inaccurate reference models for parameters neglected in the tomographic inversion will be explored in a future study.

The tomography model is parametrized using the isotropic shear wave speed parameter $V_S^2 = \frac{1}{2}(V_{SH}^2 + V_{SV}^2)$ and the radial anisotropy parameter $\zeta_S = (V_{SH}^2 - V_{SV}^2)/2V_S^2$, but for plotting purposes we plot the widely used $\xi = \frac{V_{SH}^2}{V_{SV}^2}$. We couple variations in density and isotropic *P*-wave velocity to variations in isotropic *S*-wave velocity via the scaling relationships $\mathrm{d}\ln\rho/\mathrm{d}\ln V_S = 0.4$ (Anderson *et al.* 1988) and $\mathrm{d}\ln V_P/\mathrm{d}\ln V_S = 0.5$ (Robertson & Woodhouse 1995). The sensitivity of the surface waves to other parameters, such as, for example, to the η parameter and to azimuthal anisotropy are ignored.

2.6 Linear inversion

The 3-D model parametrization used here is similar to Witek *et al.* (2021). We create a tessellated spherical grid (Wang & Dahlen 1995; Van der Lee & Nolet 1997) with nodes separated by 125 km on average at the surface. The grid centre is located at 0°N, 80°E and extends 65° in all directions. The grid is extended in depth by placing identical tessellated grids at 24 depths, which are: 25, 35, 55, 75, 95, 120, 145, 170, 200, 230, 260, 290, 320, 350, 380, 410, 450, 490, 530, 610, 660, 730, 780 and 950 km depth. We do not

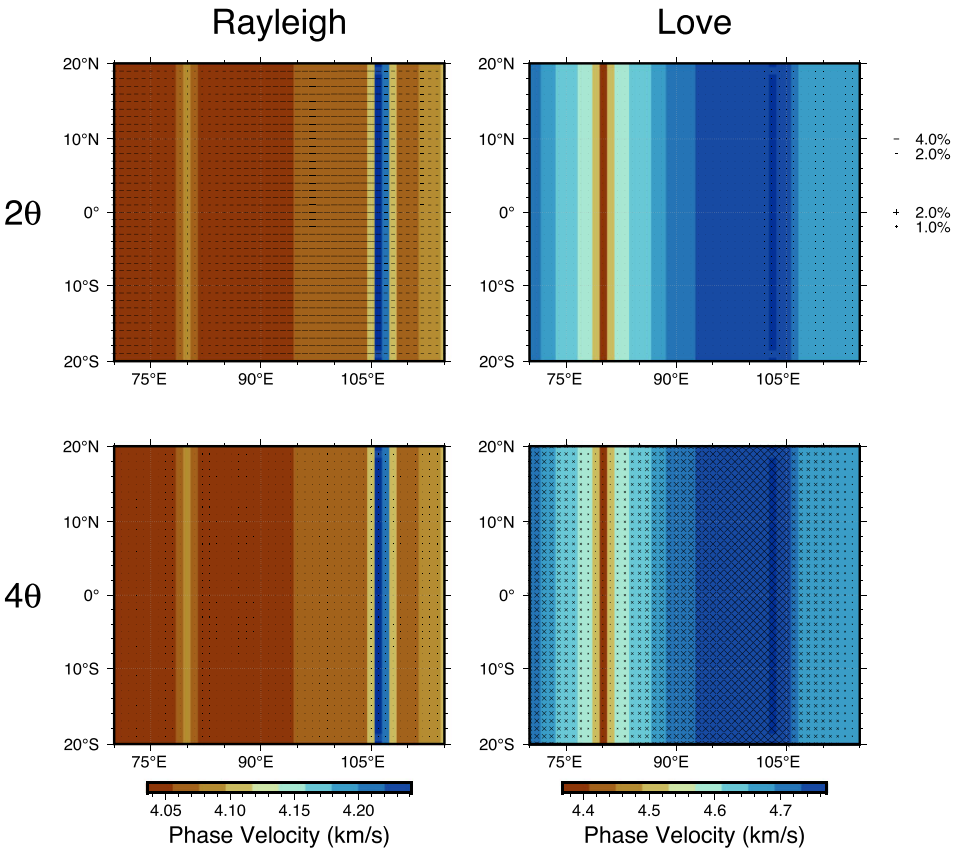

Figure 6. Phase velocities and azimuthal anisotropy perturbations for the geodynamic model calculated at 80 s period. Left-hand column shows the fundamental mode Rayleigh wave phase velocity distribution, and the right-hand column shows the fundamental mode Love wave phase velocities. Top row shows 2θ variations, and bottom row 4θ variations.

place a node at the surface in order to avoid perturbations in the crust, whose thickness and model parameters are kept fixed in this study. The 3-D model perturbations, $\delta m_i(\theta, \phi, z)$, are defined over the grid using

$$\delta m_i(\theta, \phi, z) = \sum_{j,k} \mu_{ijk} f_j(\theta, \phi) h_k(z), \tag{17}$$

where $f_j(\theta, \phi)$ is a weight derived from a triangular barycentric coordinate system using the three grid nodes j enclosing the latitude, longitude position (θ, ϕ) and $h_k(z)$ is a radial basis function at depth node k. The radial basis functions used here are triangle functions with a maximum (equal to one) at node k and linearly going to zero at nodes $k-1$ and $k+1$. Half-triangles are used for the first and last depth nodes. The basis function coefficients μ_{ijk} are determined in the inversion, and here $i = 1$ refers to $\delta \ln V_S$ and $i = 2$ refers to $\delta\zeta$.

The result of applying the automatic waveform fitting procedure to a three-component waveform is a linear combination of path average model constraints, $\boldsymbol{\eta}$, with uncorrelated uncertainties, $\Delta\boldsymbol{\eta}$ (Nolet 1990; Witek *et al.* 2023). After applying the automatic waveform fitting procedure to all ray paths in the data set, all path average model constraints $\boldsymbol{\eta}$ are collected into a single data vector $\mathbf{d}$, which is related to $\boldsymbol{\mu}$ via a linear constraints matrix G, created by projecting the eigenvectors of the Hessian from each waveform fit onto the 3-D model's basis functions. To solve for $\boldsymbol{\mu}$, we minimize a misfit function defined as

$$\mathrm{S}(\boldsymbol{\mu}) = \left(\mathrm{G}\boldsymbol{\mu} - \mathbf{d}\right)^T \mathrm{C}_e^{-1} \left(\mathrm{G}\boldsymbol{\mu} - \mathbf{d}\right) + \lambda_D^2 |\mathrm{I}\boldsymbol{\mu}|^2 + \lambda_F^2 |\mathrm{F}\boldsymbol{\mu}|^2, \tag{18}$$

where F represents the discrete horizontal gradient operator acting on $\boldsymbol{\mu}$, I is the identity matrix and C_e is a diagonal data covariance matrix of the uncorrelated uncertainties $\Delta\boldsymbol{\eta}$. We also include model norm damping (λ_D) and horizontal gradient regularization (flattening; λ_F). Optimal values are estimated by performing a trade-off-curve (i.e. L-curve) analysis. The misfit equation is optimized using up to 100 iterations of the least-squares algorithm (LSQR; Paige & Saunders 1982). After performing the tradeoff-curve analysis, the residuals are analysed and outliers are identified as those residuals more than three standard deviations away from the mean residual, which typically results in 2–3 per cent of the data set being removed. After the outliers are removed, another trade-off-curve analysis is performed for the choice of final model.

In the subsequent sections, we employ several key terms integral to the understanding of our seismic inversion methodology and interpretation of the results. For reference, here we provide concise definitions of these terms: 'model norm' refers to the magnitude of the seismic model, evaluated through the Euclidean norm of the vector representing the model. 'Damping factor' is a crucial parameter during the seismic inversion process, regulating the complexity of the resulting model. A higher value of the damping factor produces weaker tomographic models. 'Flattening factor' (or 'horizontal gradient regularization') is implemented to reduce the lateral difference of the tomographic model, particularly in the presence of high horizontal gradients. 'Variance reduction' measures how well the seismic model fits to the observed data. A high percentage of variance reduction indicates a good match between the

model and seismic data, contributing to the validity of the inversion process.

3 RESULTS

To test the ability of the inversion to recover the shear wave speed and radial anisotropy structures in the input geodynamics model, we conduct a series of synthetic inversion tests. We start by performing an initial tomography inversion, which we shall refer to as Test1, using synthetic waveforms from the ideal station distribution depicted in Fig. 3. Next, we perform two more tests, referred to as Test2 and Test3, whereby we invert 3744 waveforms computed using a station distribution (Fig. 3) obtained by selecting stations resembling a more realistic seismic data coverage. The main difference between Test2 and Test3 is the choice of regularization. The regularization used in Test2 is chosen so that the model obtained has a norm similar to that of the model chosen in Test1. On the other hand, in Test3 the regularization is chosen from the elbow of the trade-off curve between the model norm and data misfit (L-curve), as typically done in geophysical inverse problems (Aster *et al.* 2018). Fig. 7 presents latitude-averaged results from Test1, Test2 and Test3. Vertical slices through the 3-D inversion results are presented in Figs 8–10. In Table 2, we list the selected damping and flattening factors for each test and the resulting model norm and variance reduction.

By comparing the results of Test1 in Figs 7(c) and (d) with the true models in Figs 7(a) and (b), we observe similarities in both shear velocity and radial anisotropy structures. For example, the strongest low-velocity anomaly associated with the ridge is well recovered by the inversion, albeit with some smearing effects. This similarity is also seen in different cross-sections at various latitudes in Fig. 8. The same is true for the fast anomaly associated with the slab down to ∼100 km depth. While the retrieved V_S model exhibits relatively higher velocities in the vicinity of the subducted plate, the model severely underestimates the amplitude of the high-velocity anomalies below ∼100 km depth, as shown by the contours representing +1 per cent $\delta \ln V_S$ anomalies. Similarly, the inversion recovers negative radial anisotropy anomalies beneath the ridge and the trench, and a positive anomaly beneath the oceanic plate (i.e. from the ridge to the trench; Fig. 7d and Figs 8l–t). The black contours, representing +1 per cent anomalies in $\delta \ln \xi$, highlight a reasonable recovery in Test1 and Test2 of the input age-dependent positive radial anisotropy region between the ridge and the trench.

Using a more realistic station distribution strongly affects the inversion results (Figs 7e–h, 9 and 10). For example, the results of Test2 (Fig. 9)—with similar model norm to that of Test1 (see Section 2 and Table 2)—moving along the latitude, exhibits substantial differences between the input and output models both in shear wave velocity and in radial anisotropy. The output low-velocity anomaly beneath the ridge changes considerably as latitude varies from 10° to −10° (Figs 9b–j), with some artificial high-velocity anomalies appearing in some cases, which can reach a magnitude of about 2 per cent. A similar behaviour is observed for the high-velocity anomaly associated with the slab, which exhibits changes with varying latitude, showing several artificial features that are not present in the true model (e.g. Figs 9b–j). In Fig. 9, between −7.5° and 7.5° latitude, we observe the presence of an irregularly shaped high-velocity anomaly sinking in the asthenosphere parallel to the slab, appearing even stronger and clearer than the slab itself. Similarly, the output radial anisotropy varies with latitude and exhibits marked blurring effects. Nevertheless, several large-scale features of the input model are recovered, such as the signature of the subducting slab separating positive and negative ξ anomalies, as well as negative anisotropy anomalies beneath the ridge.

In the results of Test3 (Figs 7g and h and 10), that is, based on the model obtained from the elbow of the L-curve (Table 2), we observe that the output high-velocity anomaly corresponding to the slab is weaker than those obtained in Test1 and in Test2. In particular, Fig. 10(b) does not show any significant anomaly associated with the subducting slab. The retrieved radial anisotropy also varies with latitude, highlighting a decreasing resolution as we approach the edges of the study region (Figs 10l–t). Moreover, we also observe that the retrieved $\delta \ln \xi$ model is characterized by a flat positive radial anisotropy anomaly confined in the top ∼100 km depth, that is, the inversion does not recover the depth–age dependency of $\delta \ln \xi$ that is present in the input model.

4 DISCUSSION

In discussing our results, it is crucial to address the deliberate exclusions and choices made in our methodology. We intentionally omitted azimuthal anisotropy in the inversion process, as is common practice in tomographic studies as discussed in Section 2. Similarly, the choice of using a 1-D reference model in the inversion, rather than a more computationally intensive 3-D model, stems from our study's objectives and limitations of the tomographic method. However, we acknowledge the potential benefits of incorporating additional *a priori* information such as slab geometry (e.g. derived from seismicity), as well as the inclusion of azimuthal anisotropy in future studies. We recognize that these considerations can contribute to more robust and geologically consistent tomographic models, and we encourage further exploration in subsequent investigations.

4.1 Isotropic structure

In all the inversion tests performed in this study the recovered isotropic structures are characterized by two major low- and high-velocity anomalies, which broadly correspond to the ridge and to the subducting slab (Fig. 7). Overall, the ridge is well resolved, albeit some smearing effects artificially extending the output low-velocity anomaly to about 200 km depth, compared to a depth extent of ∼100 km in the input model beneath the ridge axis (Fig. 7). On the other hand, examining the +1 per cent $\delta \ln V_S$ contour lines in Fig. 7, we observe that the subducted portion of the oceanic lithosphere is imaged as a short slab hanging down to only ∼100 km of depth. This clearly highlights the limitations of the seismic data and method used in this study at imaging ∼100–200 km thick slabs. We note however that overall the slab in the true model is relatively thin and occupying a small portion of the whole study region, and thus it is naturally difficult to resolve it with current tomographic techniques. Moreover, only a few regions in the centre of the array have good azimuthal coverage (Fig. 5), which is a typical problem in tomography studies (e.g. Witek *et al.* 2023) and may lead to contamination, for example, by unmodelled azimuthal anisotropy. Furthermore, the effectiveness of the inversion process in resolving the slab is likely heavily influenced by the imposed source–receiver geometry. The arrangement and relative positioning of sources and receivers play a critical role in determining how well the inversion can reconstruct the structure of the

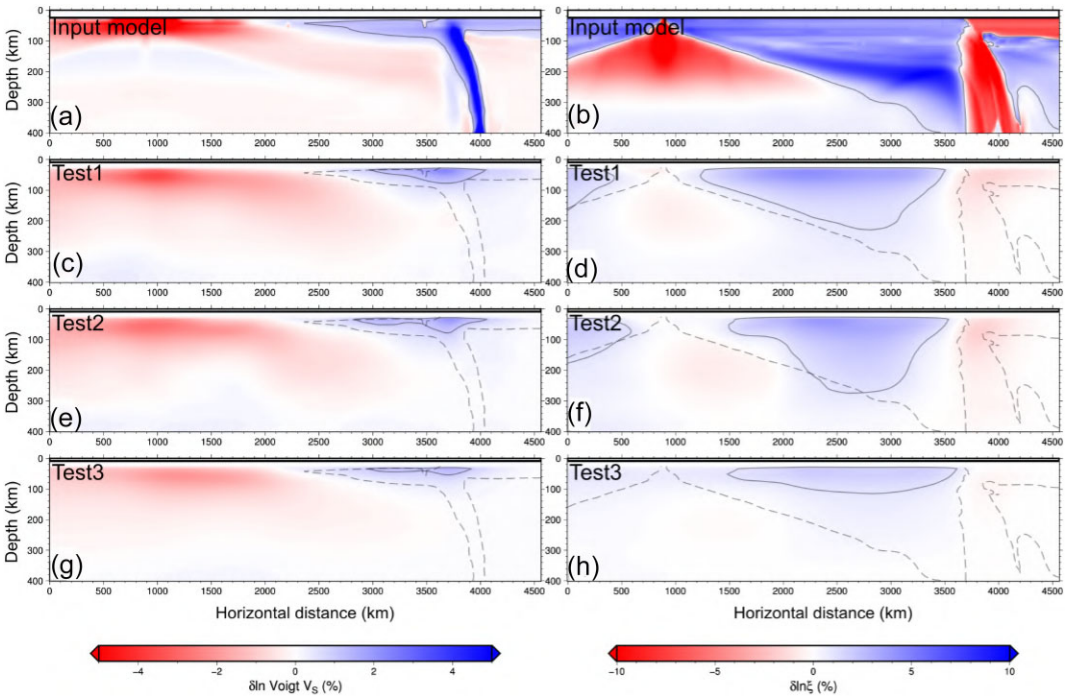

Figure 7. Results of Test1 (uniform data coverage), Test2 (realistic data coverage, same model norm as in Test1) and Test3 (realistic data coverage, regularization from L-curve's elbow). Vertical sections averaged along latitude, refer to Figs 8–10 for sections at specific latitudes. (a) True $\delta \ln V_S$ and (b) true $\delta ln\xi$ models for reference. The solid lines in (a) and (b) show the $+1$ per cent $\delta \ln V_S$ and $\delta \ln \xi$ contours outline the true slab geometry and radial anisotropy. Recovered $\delta \ln V_S$ and $\delta \ln \xi$ for (c) and (d) Test1, (e) and (f) Test2 and (g) and (h) Test3. The dashed lines correspond to $+1$ per cent $\delta \ln V_S$ and $\delta \ln \xi$ contours in the true input model, while the solid lines show the same contours for the models obtained from the tomographic inversions.

slab. Therefore, it is important to note that our results are closely tied to the specific conditions imposed during this investigation and may vary under different experimental setups. Finally, one must bear in mind that linearized ray theory is used for the modelling, whose limitations also contribute to uncertainties in the retrieved images.

Given the observed substantial degradation in resolving power with increasing depth, care should be taken when interpreting seismic tomography images, notably beneath oceanic regions. We note that for old lithospheric ages most V_S profiles in existing tomographic models exhibit a deepening of fast anomalies, which could be interpreted as a sudden and anomalous increase in lithospheric thickness (e.g. Schaeffer & Lebedev 2013; Debayle *et al.* 2016; Isse *et al.* 2019). However, our results suggest that this could be at least partly due to lateral smearing effects. Data from oceanic plates close to subduction zones and to continental passive margins should be discarded when V_S profiles from tomography models are stacked into depth–age profiles. On the other hand, the use of additional complementary data sets (e.g. further body wave phases) should enhance the resolution of the tomography images. Our rationale for this recommendation is rooted in the complex geological structures and dynamics associated with these regions, including subduction-related tectonic processes and the presence of continental passive margins. The intricate nature of these geological settings may introduce additional complexities into the seismic velocity structure, potentially leading to misleading interpretations when V_S profiles from tomography models are stacked into depth–age profiles. By carefully selecting data and excluding regions with known geological complexities, we aim to enhance the accuracy and reliability of depth–age profiles constructed from seismic tomography models. This precautionary measure is essential to ensure that interpretations regarding lithospheric thickness variations are not confounded by lateral smearing effects associated with specific geological settings.

Overall, the age-dependent gradual thickening of the lithosphere can be inferred from all the output isotropic V_S models, which is consistent with the imposed thermal structure based on the HSCM (Section 2.1; Turcotte & Schubert 2014). However, the transition from the high-velocity lithosphere to the underlying low-velocity asthenosphere is much more discontinuous in models with a realistic station distribution (Test2 and Test3; see, e.g. Fig. 9).

4.2 Radially anisotropic structure

In an upper mantle dominated by A-type olivine textures, horizontally and vertically oriented fabrics result in positive ($V_{SV} < V_{SH}$) and negative ($V_{SV} > V_{SH}$) radial anisotropy (Karato *et al.* 2008), respectively, which can be used to infer patterns of mantle flow. Our tomography inversion tests show a good first-order recovery of the broad radial anisotropy features in the input models. This suggests little contamination from the more general unmodelled anisotropy encapsulated in the 21 elastic constants used to compute the input synthetic seismograms. In particular, small negative perturbations in ξ are found in Test1 and Test2 beneath the ridge and in the slab's region. In contrast, Test3 does not recover any substantial negative ξ anomalies. This stresses the strong impact that regularization can have on inferences of the vertical components of mantle flow. Radial anisotropy results are generally well retrieved although in

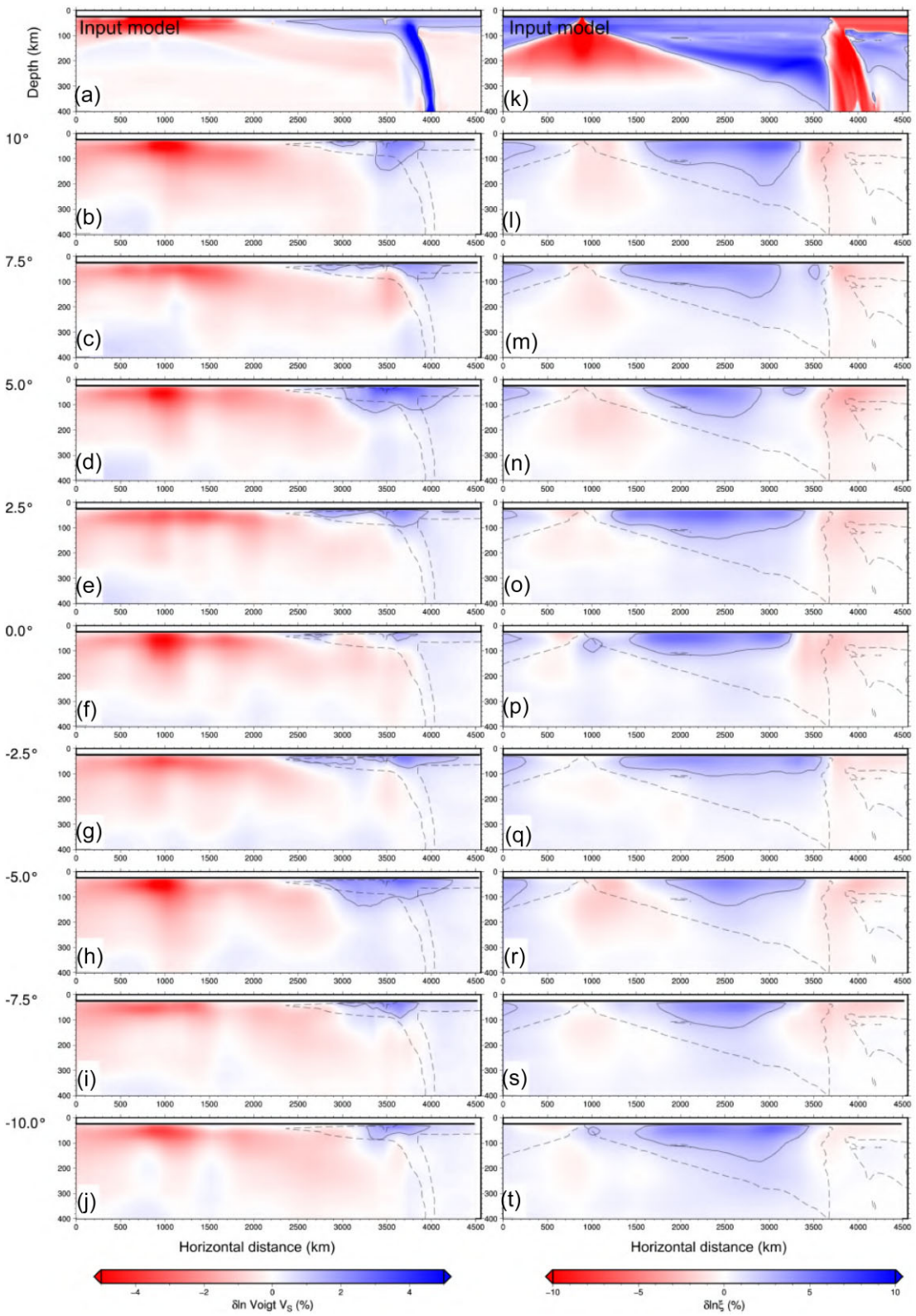

Figure 8. Results of Test1. (a) and (k) Top panels are the true $\delta \ln V_S$ and $\delta \ln \xi$ models for reference. $+1$ per cent $\delta \ln V_S$ and $\delta \ln \xi$ contours outline the true slab geometry and radial anisotropy. (b)–(j) are the recovered $\delta \ln V_S$ and (l)–(t) are the recovered $\delta ln \xi$ at different latitudes. The $+1$ per cent $\delta \ln V_S$ and $\delta \ln \xi$ contours are drawn in black on the (b)–(j) left-hand panel and (l)–(t) right-hand panel, respectively, for the true model (dashed line) and the obtained result (solid line).

our inversions we approximate the 21 elastic parameters to only 5, that is, neglecting azimuthal anisotropy despite the fact that this reaches values up to 2.7 per cent in some areas of the geodynamic model. This is true even when we assume a realistic distribution of events and receivers (i.e. Test2 and Test3). However, ignoring the azimuthal anisotropy may cause smearing effects and artifacts

Table 2. Trade-off curves from PWI. In column, the model norm, (vr) variance reduction, (λ_d) damping factor, (λ_{f1}) flattening factor for V_S, (λ_{f2}) flattening factor for ζ. In bold, the regularization factors selected for the best result of Test1, Test2 and Test3.

	Ideal station distribution				
	Norm	vr (per cent)	λ_d	λ_{f1}	λ_{f2}
	11.36	87.6	0.0	0.0	0.0
	11.11	87.6	0.001	0.0008	0.0008
	11.08	87.6	0.001	0.001	0.001
	11.04	87.6	0.001	0.0012	0.0012
	10.52	87.6	0.003	0.0024	0.0024
	10.27	87.6	0.003	0.003	0.003
	10.06	87.6	0.003	0.0036	0.0036
	8.09	87.2	0.01	0.008	0.008
	7.80	87.04	0.01	0.01	0.01
	7.58	86.8	0.01	0.012	0.012
	5.33	85.3	0.03	0.024	0.024
	5.17	84.9	0.03	0.03	0.03
	5.02	84.5	0.03	0.036	0.036
	2.79	79.3	0.1	0.08	0.08
Test1	**2.72**	**78.7**	**0.1**	**0.1**	**0.1**
	2.67	78.1	0.1	0.12	0.12
	1.34	67.1	0.3	0.24	0.24
	1.33	66.5	0.3	0.3	0.3
	1.31	66.03	0.3	0.36	0.36
	0.41	41.01	1.0	0.8	0.8
	0.409	40.5	1.0	1.0	1.0
	0.408	40.04	1.0	1.2	1.2
	0.103	18.06	3.0	2.4	2.4
	0.1	16.9	3.0	3.0	3.0
	0.097	16.03	3.0	3.6	3.6
	Real station distribution				
	Norm	vr (per cent)	λ_d	λ_{f1}	λ_{f2}
	4.97	99.2	0.001	0.0008	0.0008
	4.97	99.2	0.001	0.001	0.001
	4.97	99.2	0.001	0.0012	0.0012
	4.99	99.2	0.003	0.0024	0.0024
	4.99	99.2	0.003	0.003	0.003
	5.01	99.2	0.003	0.0036	0.0036
	4.90	99.2	0.01	0.008	0.008
	4.89	99.2	0.01	0.01	0.01
	4.93	99.2	0.01	0.012	0.012
	4.34	99.1	0.03	0.024	0.024
	4.22	99.1	0.03	0.03	0.03
	4.10	99.1	0.03	0.036	0.036
	2.86	98.8	0.1	0.08	0.08
Test2	**2.80**	**98.7**	**0.1**	**0.1**	**0.1**
	2.77	98.7	0.1	0.12	0.12
	1.54	97.8	0.3	0.24	0.24
Test3	**1.54**	**97.7**	**0.3**	**0.3**	**0.3**
	1.54	97.7	0.3	0.36	0.36
	0.680	95.3	1.0	0.8	0.8
	0.692	95.2	1.0	1.0	1.0
	0.704	95.0	1.0	1.2	1.2
	0.429	91.1	3.0	2.4	2.4
	0.439	90.4	3.0	3.0	3.0
	0.449	89.7	3.0	3.6	3.6
	0.184	61.0	10.0	8.0	8.0
	0.178	57.2	10.0	10.0	10.0
	0.172	53.9	10.0	12.0	12.0

observed, for example, in the case of Test2 and Test3 (see Figs 9 and 10).

Overall Test1 and Test2 show a reasonable recovery of the age-dependent distribution of positive radial anisotropy (Figs 7d and f). This is due to the gradual thickening of the lithosphere as described by the HSCM and the resulting deepening of the low-viscosity, highly anisotropic asthenospheric channel. In contrast, Test3 exhibits a different, age-independent anisotropy structure, resembling that predicted by the plate cooling model (Parson & McKenzie 1977, Fig. 7h). The results from Test3 are consistent with most of the existing radial anisotropy regional and global scale models (e.g. Beghein *et al.* 2014; Burgos *et al.* 2014; Chang *et al.* 2015; Schaeffer *et al.* 2016; Debayle *et al.* 2016), which do not show any significant age–depth dependency at lithospheric depths. These models tend to be characterized by an upper layer where $V_{SV} > V_{SH}$ and a lower layer where $V_{SV} < V_{SH}$, with a transition that occurs at about the same depth of ∼60–80 km for all lithospheric ages (Nettles & Dziewonski 2008; French *et al.* 2013; Auer *et al.* 2014; Beghein *et al.* 2014; Burgos *et al.* 2014; Chang *et al.* 2015). A similar result was found by Beghein *et al.* (2019) by applying a Bayesian inversion approach to three published Pacific surface wave dispersion data sets. In these models, the recovered radial anisotropy structures differ even in pattern and, in contrast to models of isotropic V_S and azimuthal anisotropy, display no obvious age dependence. However, given the large uncertainties in the inversions, the authors concluded that radial anisotropy, azimuthal anisotropy and velocity models could actually reflect compatible, age-dependent, lithosphere–asthenosphere boundary depth estimates as expected from the HSCM. More recently, Kendall *et al.* (2022) compared a 2-D geodynamic ridge model with seismological observations and applied a tomographic filter to the geodynamic model. They concluded that strong regularization likely controls the flattening of observed depth–age trends in radial anisotropy, which is confirmed by our waveform analysis.

4.3 Half-space versus plate cooling models

The obtained distributions of radial anisotropy resembling either the HSCM (Test1 and Test2) or the plate cooling model (Test3) clearly show how small changes in the inversion parameters (e.g. regularization) can cause large changes in the tomographic result, especially for models with a sparse, realistic distribution of receivers. In turn, this can have major implications for the interpretation of the models in terms of Earth's dynamics and cooling. The plate cooling model has been frequently invoked to explain the age-independent trend of surface heat flux and bathymetry observed for seafloor ages >70–80 Myr. Mechanisms that would explain an age-independent thermal structure of the oceanic lithosphere are plate erosion by bottom heating or plate delamination by small-scale convection or by plume-lithosphere interaction (Stein & Stein 1992; Parson & McKenzie 1978). The success of the plate cooling model in explaining these surface observables depends, however, entirely on the use of an artificial boundary condition at the bottom, which comprises two free parameters, plate thickness and basal temperature (Korenaga *et al.* 2021). There is no such boundary in the real mantle with a constant temperature, but these free parameters allow the plate model to be flexible enough to fit observations on older seafloor. More recently, Korenaga *et al.* (2021) proposed an updated version of the classic HSCM. By incorporating the effects of incomplete viscous relaxation, *P–T* dependent physical parameters, radiogenic heating and mainly secular cooling the authors were able to predict

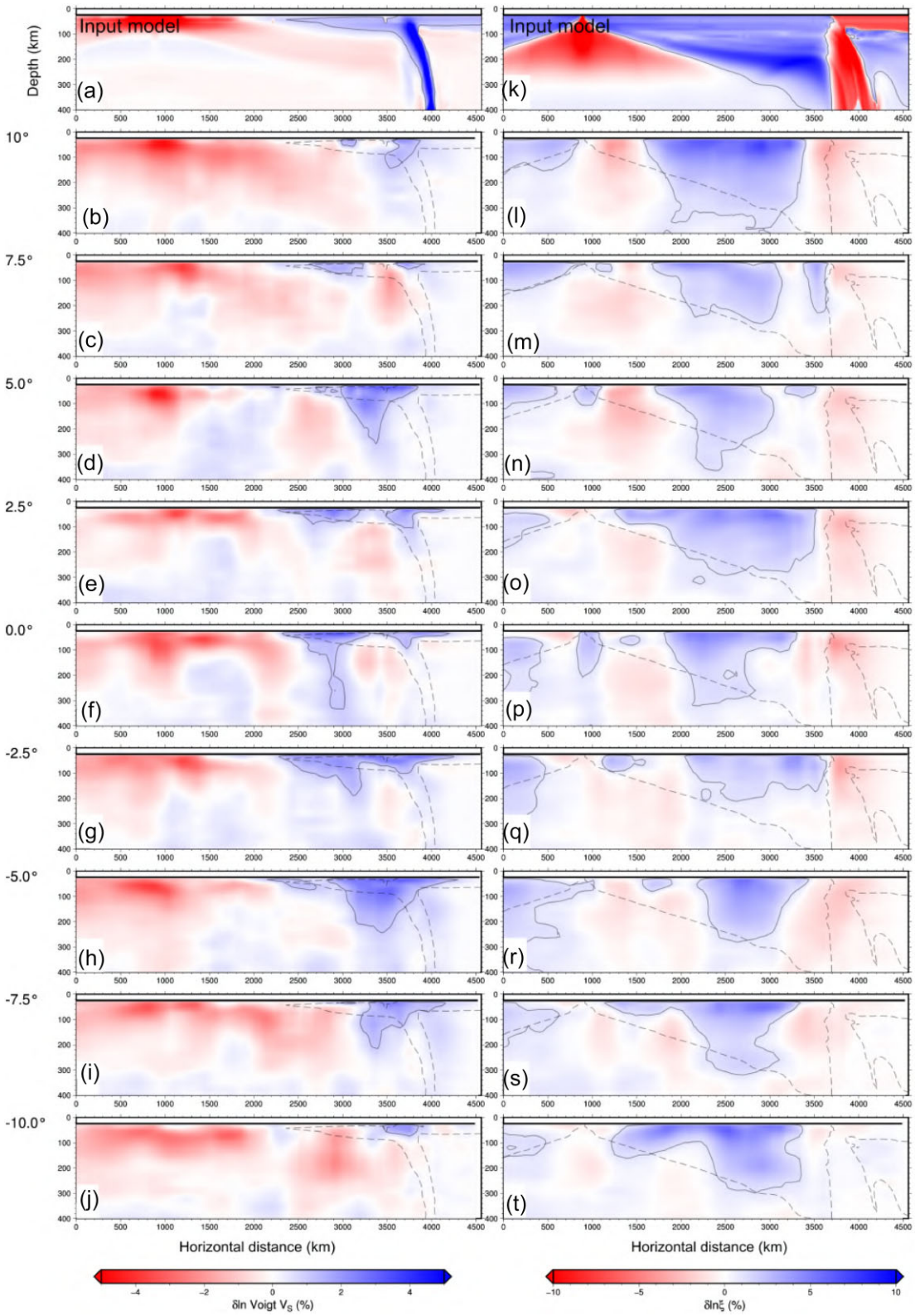

Figure 9. Results of Test2 with similar model norm to Test1 showed in Fig. 8. Velocity variations and radial anisotropy are plotted as in Fig. 8.

the thickening of the lithosphere together with the bathymetry and surface heat fluxes. The authors, however, do not provide an explanation for the age-independency of the radial anisotropy profiles in current tomography models. Similar to Beghein *et al.* (2019) and to Kendall *et al.* (2022), here we conclude that radial anisotropy models are likely poorly constrained and could be in fact consistent with the HSCM. Enhanced data coverage, notably from large-scale deployments of ocean bottom seismometers (e.g. Pacific

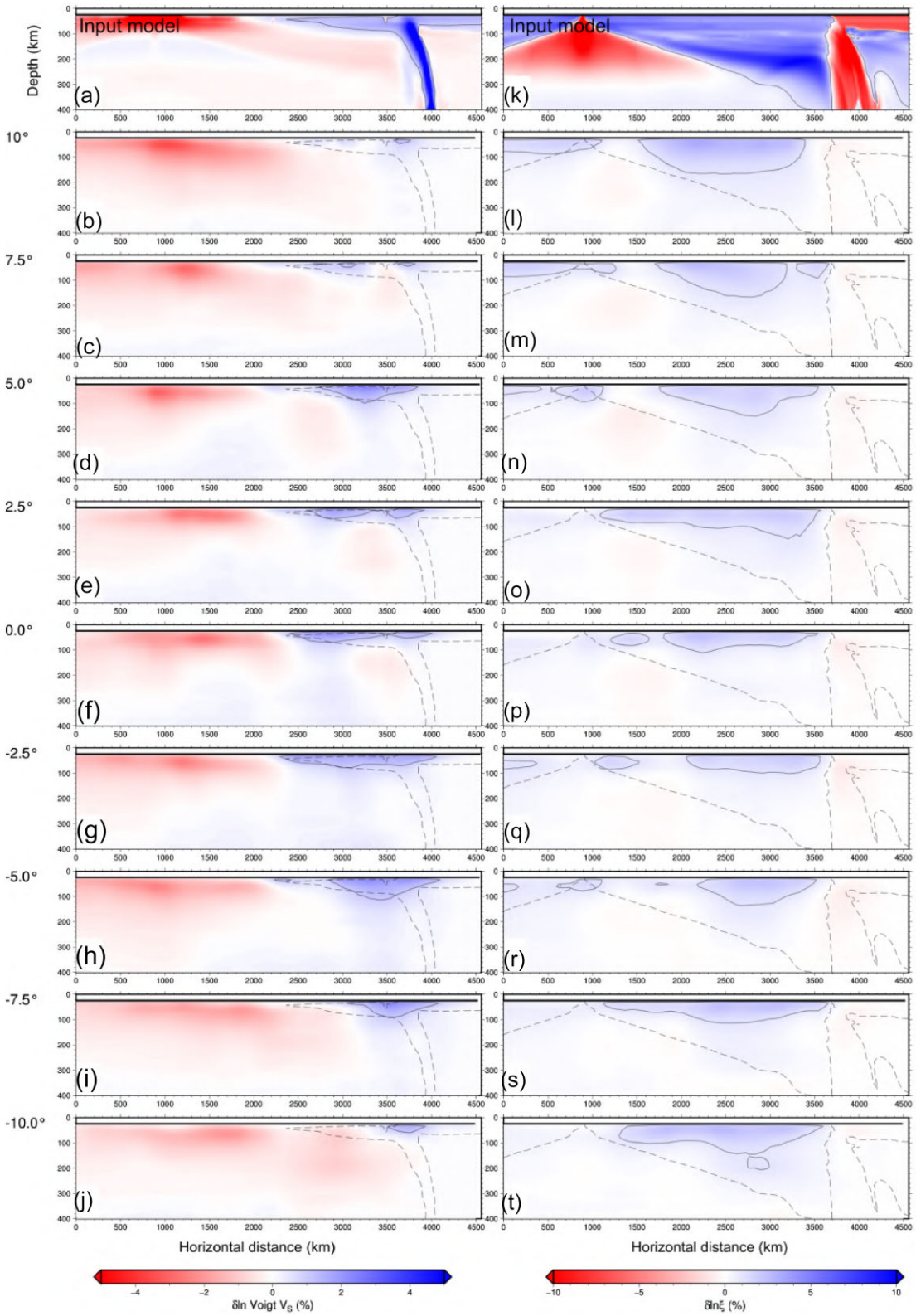

Figure 10. Results of Test3, a reasonable model based on L-curve 'corner' trade'-off criteria. Velocity variations and radial anisotropy are plotted as in Fig. 8.

Array, http://eri-ndc.eri.u-tokyo.ac.jp/PacificArray/; Rhum-rum, Barruol & Sigloch (2013)—https://www.rhum-rum.net/en/; UP-FLOW, https://upflow-eu.github.io/) are necessary to improve the resolution of (an)isotropic models beneath the oceans.

4.4 Anisotropy at lithospheric depths

Differently from radial anisotropy models that display negative radial anisotropy in the upper 60–80 km of the oceanic lithosphere (Nettles & Dziewonski 2008; Beghein *et al.* 2014;

Burgos *et al.* 2014), our inversions show $V_{SH} > V_{SV}$ also at lithospheric depths. This could be ascribed to, for example, melt-assisted deformational processes occurring at the ridge yielding fabrics different from those modelled here (Holtzman *et al.* 2003; Kaminski 2006; Hansen *et al.* 2016), and/or to a different corner flow dynamics at the ridge (as an example, Hedjazian *et al.* 2017, obtained a weakly positive radial anisotropy within the lithosphere due to a more inclined fabrics than in our model). Recent studies based on local ocean–bottom seismic arrays deployed in areas not affected by upwelling plumes found that radial anisotropy is actually positive ($\xi \geq 5$ per cent) in the shallow oceanic lithosphere down to at least 30 km below the seafloor (Russel *et al.* 2018). Thus, the negative ξ retrieved at lithospheric depths in plate- and global-scale surface wave models might be related to the fact that these surface wave studies have not included the high-frequency data required to resolve anisotropy at shallow depths (Hansen *et al.* 2016; Chang & Ferreira 2017).

5 CONCLUSIONS

We combined geodynamic simulations with seismological forward and inverse modelling to investigate which realistic upper-mantle isotropic and anisotropic features can and cannot be resolved with classical tomography methods. We used the automatic PWI method of Witek *et al.* (2023) to perform seismic tomography inversions of ∼52 080 synthetic waveforms computed using the SEM for a realistic 3-D Earth model obtained from geodynamics simulations and fabrics calculations. The 3-D geodynamic model reproduces a geological setting composed by an oceanic ridge, in the middle of the modelling domain, and two subduction zones, to the western and eastern sides of the domain. We tested ideal and more realistic seismic station coverages, which showed the strengths and limitations of the tomographic inversions. The models of isotropic V_S and radial anisotropy that we obtained from the PWI inversions show that the tomographic result is strongly influenced both by the data coverage and the model regularization. While changes in station coverage can cause some distortions in the retrieved isotropic and radially anisotropic structures, the large-scale features can still be resolved by applying less regularization than in typical real tomography inversions. On the other hand, by applying the L-curve 'corner' trade'-off criteria to select regularization, which is typically used in tomography inversions, leads to substantial artefacts in the resulting tomographic images. For example, by changing regularization one can obtain anisotropic models similar to the HSCM, showing age-dependent lithospheric structures, or, conversely, obtain results similar to the plate cooling model, characterized by flat and age-independent lithospheric structures. Moreover, in all cases, the retrieved subducted slabs can be strongly distorted, showing substantial artificial thickening and also losing a clear fast velocity signature below ∼ 100 km depth. Future work combining surface wave data with higher frequency body wave data should help resolve these issues. Furthermore, efforts to continue enhancing seismic data coverage are essential, notably to cover the Earth's oceans, such as with large-scale ocean–bottom seismometer deployments (e.g. PacificArray, https://eri-ndc.eri.u-tokyo.ac.jp/PacificArray/, Rhum-rum experiment—Barruol & Sigloch (2013), https://www.rhum-rum.net/en/, UPFLOW, https://upflow-eu.github.io). Finally, we note that while our source-receiver configuration is designed to resemble those employed in similar real data studies, and our conclusions can be cautiously extended to somewhat broader scenarios, it is crucial to emphasize that the results presented here remain anchored to the specific conditions imposed in this study. Interpretation of our findings should therefore be within the framework of this specific setup, recognizing the nuanced interplay between the imposed constraints and the generalizability of our seismic anisotropy tomography outcomes. Moreover, we emphasize that this study focuses on waveform tomography whereby the sources and receivers are all within the same tomography box (which is the case of many regional tomographic inversions).

ACKNOWLEDGMENTS

We want to express our sincere thanks to the editor Huajian Yao for their guidance and support during the review process. We are grateful to an anonymous reviewer and Jiashun Hu for their invaluable insights and constructive comments that have significantly enhanced the quality of this work. AMGF is grateful to funding support from NERC grant NE/N011791/1 and from the European Research Council (ERC) under the European Union's Horizon 2020 research and innovation programme (grant agreement no. 101001601, UPFLOW project). SJC was supported by Basic Science Research Program through the National Research Foundation of Korea (NRF) funded by the Ministry of Education (no. 2019R1A6A1A03033167). FR and MF were supported by the ERC StG 758199 NEWTON.

DATA AVAILABILITY

The D-Rex code used for the fabric modelling can be found inside the ECOMAN software package (https://newtonproject.geoscienze.unipd.it/ecoman/). Paraview was used for graphic visualization of the model output (https://www.paraview.org/). SPECFEM3D_GLOBE is available on github (https://github.com/geodynamics/specfem3d_globe.git) and Zenodo archive (https://doi.org/10.5281/zenodo.7756944).

SUPPORTING INFORMATION

Supplementary data are available at *GJI* online.

suppl_data

Please note: Oxford University Press is not responsible for the content or functionality of any supporting materials supplied by the authors. Any queries (other than missing material) should be directed to the corresponding author for the paper.

REFERENCES

Aki, K., 1980. *Quantitative Seismology, Theory and Methods,* Vol. **1**. Freeman, San Francisco, p. 557.

Anderson, D.L., 1961. Elastic wave propagation in layered anisotropic media, *J. geophys. Res.,* **66**(9), 2953–2963.

Anderson, O.L., Schreiber, E., Liebermann, R.C. & Soga, N., 1988. Some elastic constant data on minerals relevant to geophysics. *Elastic Properties and Equations of State,* Vol. **26**. American Geophysical Union, Washington, DC, pp. 237–270.

Aster, R.C., Borchers, B. & Thurber, C.H., 2018. *Parameter Estimation and Inverse Problems,* Elsevier.

Auer, L., Boschi, L., Becker, T., Nissen-Meyer, T. & Giardini, D., 2014. Savani: a variable resolution whole-mantle model of anisotropic shear velocity variations based on multiple data sets, *J. geophys. Res.: Solid Earth,* **119**(4), 3006–3034.

Bai, Q., Mackwell, S. & Kohlstedt, D., 1991. High-temperature creep of olivine single crystals 1. mechanical results for buffered samples, *J. geophys. Res.: Solid Earth,* **96**(B2), 2441–2463.

Barruol, G. & Sigloch, K., 2013. Investigating la réunion hot spot from crust to core, *EOS, Trans. Am. geophys. Un.,* **94**(23), 205–207.

Beghein, C., Yuan, K., Schmerr, N. & Xing, Z., 2014. Changes in seismic anisotropy shed light on the nature of the Gutenberg discontinuity, *Science,* **343,** 1237–1240.

Beghein, C., Xing, Z. & Goes, S., 2019. Thermal nature and resolution of the lithosphere–asthenosphere boundary under the pacific from surface waves, *J. geophys. Int.,* **216,** 1441–1465.

Boneh, Y., Morales, L.F., Kaminski, E. & Skemer, P., 2015. Modeling olivine cpo evolution with complex deformation histories: implications for the interpretation of seismic anisotropy in the mantle, *Geochem. Geophys. Geosyst.,* **16**(10), 3436–3455.

Burgos, G., Montagner, J.-P., Capdeville, Y., Mocquet, A. & Drilleau, M., 2014. Oceanic lithosphere-asthenosphere boundary from surface wave dispersion data, *J. geophys. Res.: Solid Earth,* **119**(2), 1079–1093.

Chang, S.-J. & Ferreira, A.M., 2017. Improving global radial anisotropy tomography: the importance of simultaneously inverting for crustal and mantle structure, *Bull. seism. Soc. Am.,* **107**(2), 624–638.

Chang, S.-J. & Ferreira, A.M., 2019. Inference on water content in the mantle transition zone near subducted slabs from anisotropy tomography, *Geochem. Geophys. Geosyst.,* **20**(2), 1189–1201.

Chang, S.-J., Ferreira, A.M., Ritsema, J., van Heijst, H.J. & Woodhouse, J.H., 2014. Global radially anisotropic mantle structure from multiple datasets: a review, current challenges, and outlook, *Tectonophysics,* **617,** 1–19.

Chang, S.-J., Ferreira, A.M., Ritsema, J., van Heijst, H.J. & Woodhouse, J.H., 2015. Joint inversion for global isotropic and radially anisotropic mantle structure including crustal thickness perturbations, *J. geophys. Res.: Solid Earth,* **120**(6), 4278–4300.

Chang, S.-J., Ferreira, A.M. & Faccenda, M., 2016. Upper-and mid-mantle interaction between the Samoan plume and the Tonga–Kermadec slabs, *Nat. Commun.,* **7**(1), 1–9.

Chen, M. & Tromp, J., 2007. Theoretical and numerical investigations of global and regional seismic wave propagation in weakly anisotropic earth models, *J. geophys. Int.,* **168**(3), 1130–1152.

Dahlen, F.A. & Tromp, J., 2021. *Theoretical Global Seismology,* Princeton University Press.

Debayle, E., Dubuffet, F. & Durand, S., 2016. An automatically updated s-wave model of the upper mantle and the depth extent of azimuthal anisotropy, *Geophys. Res. Lett.,* **43,** 674–682.

Durham, W. & Goetze, C., 1977. Plastic flow of oriented single crystals of olivine: 1. mechanical data, *J. geophys. Res.,* **82**(36), 5737–5753.

Dziewoński, A.M. & Anderson, D.L., 1981. Preliminary reference Earth model, *Phys. Earth planet. Inter.,* **25,** 297–356.

Evans, B. & Goetze, C., 1979. The temperature variation of hardness of olivine and its implication for polycrystalline yield stress, *J. geophys. Res.,* **84,** 5505–5524.

Faccenda, M., 2014. Mid mantle seismic anisotropy around subduction zones, *Phys. Earth planet. Inter.,* **227,** 1–19.

Faccenda, M. & Capitanio, F.A., 2013. Seismic anisotropy around subduction zones: Insights from three-dimensional modeling of upper mantle deformation and sks splitting calculations, *Geochem. Geophys. Geosyst.,* **14**(1), 243–262.

Ferreira, A.M., Faccenda, M., Sturgeon, W., Chang, S.-J. & Schardong, L., 2019. Ubiquitous lower-mantle anisotropy beneath subduction zones, *Nat. Geosci.,* **12**(4), 301–306.

French, S. & Romanowicz, B.A., 2014. Whole-mantle radially anisotropic shear velocity structure from spectral-element waveform tomography, *J. geophys. Int.,* **199**(3), 1303–1327.

French, S., Lekic, V. & Romanowicz, B., 2013. Waveform tomography reveals channeled flow at the base of the oceanic asthenosphere, *Science,* **342**(6155), 227–230.

Gerya, T., 2019. *Introduction to Numerical Geodynamic Modelling,* Cambridge University Press.

Gerya, T. & Yuen, D.A., 2003. Characteristics-based marker-in-cell method with conservative finite-differences schemes for modeling geological flows with strongly variable transport properties, *Phys. Earth planet. Inter.,* **140**(4), 293–318.

Goforth, T. & Herrin, E., 1979. Phase-matched filters: application to the study of Love waves, *Bull. seism. Soc. Am.,* **69**(1), 27–44.

Goldstein, P. & Snoke, A., 2005. SAC availability for the IRIS Community, *Incorporated Institutions for Seismology Data Management Center Electronic Newsletter,* Vol. **7**(UCRL-JRNL-211140).

Hansen, L., Qi, C. & Warren, J., 2016. Olivine anisotropy suggests gutenberg discontinuity is not the base of the lithosphere, *Proc. Natl. Acad. Sci.,* **113**(38), 10503–10506.

Hansen, L.N., Zhao, Y.-H., Zimmerman, M.E. & Kohlstedt, D.L., 2014. Protracted fabric evolution in olivine: implications for the relationship among strain, crystallographic fabric, and seismic anisotropy, *Earth planet. Sci. Lett.,* **387,** 157–168.

Hanson, D.R. & Spetzler, H.A., 1994. Transient creep in natural and synthetic, iron-bearing olivine single crystals: mechanical results and dislocation microstructures, *Tectonophysics,* **235**(4), 293–315.

Hedjazian, N., Garel, F., Rhodri Davies, D. & Kaminski, E., 2017. Age-independent seismic anisotropy under oceanic plates explained by strain history in the asthenosphere, *Earth planet. Sci. Lett.,* **460,** 135–142.

Herrin, E. & Goforth, T., 1977. Phase-matched filters: application to the study of Rayleigh waves, *Bull. seism. Soc. Am.,* **67**(5), 1259–1275.

Holtzman, B.K., Kohlstedt, D.L., Zimmerman, M.E., Heildelbach, F., Hiraga, T. & Hustoft, J., 2003. Olivine anisotropy suggests Gutenberg discontinuity is not the base of the lithosphere, *Science,* **301,** 1227–1230.

Isse, T. *et al.*, 2019. Surface wave tomography for the pacific ocean incorporating seafloor seismic observations and plate thermal evolution, *Earth planet. Sci. Lett.,* **510,** 116–130.

Jin, Z., Bai, Q. & Kohlstedt, D., 1994. High-temperature creep of olivine crystals from four localities, *Phys. Earth planet. Inter.,* **82**(1), 55–64.

Kaminski, E., 2006. Interpretation of seismic anisotropy in terms of mantle flow when melt is present, *Geophys. Res. Lett.,* **33**(2). https://doi.org/10.1029/2005GL024454.

Kaminski, E., Ribe, N.M. & Browaeys, J.T., 2004. D-rex, a program for calculation of seismic anisotropy due to crystal lattice preferred orientation in the convective upper mantle, *J. geophys. Int.,* **158**(2), 744–752.

Karato, S.-I. & Wu, P., 1993. Rheology of the upper mantle: a synthesis, *Science,* **260**(5109), 771–778.

Karato, S.-I., Jung, H., Katayama, I. & Skemer, P., 2008. Geodynamic significance of seismic anisotropy of the upper mantle: new insights from laboratory studies, *Annu. Rev. Earth Planet. Sci.,* **36,** 59–95.

Katayama, I., &, 2008. Low-temperature, high-stress deformation of olivine under water-saturated conditions, *Phys. Earth planet. Inter.,* **168,** 125–133.

Kendall, E., Ferreira, A.M., Chang, S.-J., Witek, M. & Peter, D., 2021. Constraints on the upper mantle structure beneath the pacific from 3-d anisotropic waveform modeling, *J. geophys. Res.: Solid Earth,* **126**(4), e2020JB020003. https://doi.org/10.1029/2020JB020003.

Kendall, E., Faccenda, M., Ferreira, A. & Chang, S.-J., 2022. On the relationship between oceanic plate speed, tectonic stress, and seismic anisotropy, *Geophys. Res. Lett.,* **49**(15), e2022GL097795. https://doi.org/10.1029/2022GL097795.

Kissling, E., Ellsworth, W.L., Eberhart-Phillips, D. & Kradolfer, U., 1994. Initial reference models in local earthquake tomography, *J. geophys. Res.: Solid Earth,* **99**(B10), 19635–19646.

Kohlstedt, D. & Goetze, C., 1974. Low-stress high-temperature creep in olivine single crystals, *J. geophys. Res.,* **79**(14), 2045–2051.

Komatitsch, D. & Tromp, J., 1999. Introduction to the spectral element method for three-dimensional seismic wave propagation, *J. geophys. Int.,* **139**(3), 806–822.

Korenaga, T., Korenaga, J., Kawakatsu, H. & Yamano, M., 2021. A new reference model for the evolution of oceanic lithosphere in a cooling earth, *J. geophys. Res.: Solid Earth,* **126**(6), e2020JB021528. https://doi.org/10.1029/2020JB021528.

Kustowski, B., Ekstrom, G. & Dziewonski, A., 2008. Anisotropic shear-wave velocity structure of the earth's mantle: a global model, *J. geophys. Res.: Solid Earth,* **113**(B6). https://doi.org/10.1029/2007JB005169.

Lebedev, S., Nolet, G., Meier, T. & van der Hilst, R.D., 2005. Automated multimode inversion of surface and S waveforms, *J. geophys. Int.,* **162,** 951–964.

Lo Bue, R., Faccenda, M. & Yang, J., 2021. The role of adria plate lithospheric structures on the recent dynamics of the central mediterranean region, *J. geophys. Res.: Solid Earth,* **126**(10), e2021JB022377. https://doi.org/10.1029/2021JB022377.

Lo Bue, R., Rappisi, F., Vanderbeek, B.P. & Faccenda, M., 2022. Tomographic image interpretation and central-western mediterranean-like upper mantle dynamics from coupled seismological and geodynamic modeling approach, *Front. Earth Sci.,* **10,** 884100. https://doi.org/10.3389/feart.2022.884100.

Love, A. E.H., 1927. *A Treatise on the Theory of Elasticity,* Cambridge University Press.

Marquering, H. & Snieder, R., 1995. Surface-wave mode coupling for efficient forward modelling and inversion of body-wave phases, *J. geophys. Int.,* **120**(1), 186–208.

Montagner, J.-P. & Nataf, H.-C., 1986. A simple method for inverting the azimuthal anisotropy of surface waves, *J. geophys. Res.,* **91**(B1), 511–520.

Montagner, J.-P. & Nataf, H.-C., 1988. Vectorial tomography - I. Theory, *J. geophys. Int.,* **94**(2), 295–307.

Moulik, P. & Ekström, G., 2014. An anisotropic shear velocity model of the Earth's mantle using normal modes, body waves, surface waves and long-period waveforms, *J. geophys. Int.,* **199**(3), 1713–1738.

Nettles, M. & Dziewonski, A., 2008. Radially anisotropic shear velocity structure of the upper mantle globally and beneath north america, *J. geophys. Res.: Solid Earth,* **113**(B2). https://doi.org/10.1029/2006JB004819.

Nicolas, A., Boudier, F. & Boullier, A., 1973. Mechanisms of flow in naturally and experimentally deformed peridotites, *Am. J. Sci.,* **273**(10), 853–876.

Nolet, G., 1990. Partitioned waveform inversion and two-dimensional structure under the network of autonomously recording seismographs, *J. geophys. Res.,* **95**(B6), 8499–8512.

Paige, C.C. & Saunders, M.A., 1982. Algorithm 583: Lsqr: sparse linear equations and least squares problems, *ACM Trans. Math. Softw. (TOMS),* **8**(2), 195–209.

Panning, M.P., Lekić, V. & Romanowicz, B.A., 2010. Importance of crustal corrections in the development of a new global model of radial anisotropy, *J. geophys. Res.: Solid Earth,* **115**(B12). https://doi.org/10.1029/2010JB007520.

Park, J. & Levin, V., 2002. Seismic anisotropy: tracing plate dynamics in the mantle, *Science,* **296**(5567), 485–489.

Parson, B. & McKenzie, D., 1977. An analysis of the variation of ocean floor bathymetry and heat flow with age, *J. geophys. Res.: Solid Earth,* **82(5),** 803–827.

Parson, B. & McKenzie, D., 1978. Mantle convection and the thermal structure of the plates, *J. geophys. Res.: Solid Earth,* **83,** 4485–4496.

Raleigh, C., Kirby, S., Carter, N. & Lallemant, H.A., 1971. Slip and the clinoenstatite transformation as competing rate processes in enstatite, *J. geophys. Res.,* **76**(17), 4011–4022.

Ranalli, G., 1995. *Rheology of the Earth,* Springer Science & Business Media.

Rappisi, F. & Faccenda, M., 2019. Geodynamic and seismological numerical modelling for seismic anisotropy studies, *AGUFM,* **2019,** DI21B–0038.

Ritsema, J., Deuss, A., Van Heijst, H.J. & Woodhouse, J.H., 2011. S40RTS: a degree-40 shear-velocity model for the mantle from new Rayleigh wave dispersion, teleseismic traveltime and normal-mode splitting function measurements, *J. geophys. Int.,* **184**(3), 1223–1236.

Robertson, G. & Woodhouse, J., 1995. Evidence for proportionality of p and s heterogeneity in the lower mantle, *J. geophys. Int.,* **123**(1), 85–116.

Ronchi, C., Iacono, R. & Paolucci, P.S., 1996. The "cubed sphere": a new method for the solution of partial differential equations in spherical geometry, *J. Comput. Phys.,* **124**(1), 93–114.

Russel, J., Gaherty, J., Lin, P.-Y., Lizarradle, D., Collins, J., Hirth, G. & Evans, R., 2018. High-resolution constraints on pacific upper mantle petrofabric inferred from surface-wave anisotropy, *J. geophys. Res.: Solid Earth,* **124,** 631–657.

Sadourny, R., 1972. Conservative finite-difference approximations of the primitive equations on quasi-uniform spherical grids, *Mon. Weather Rev.,* **100**(2), 136–144.

Schaeffer, A. & Lebedev, S., 2013. Global shear speed structure of the upper mantle and transition zone, *J. geophys. Int.,* **194**(1), 417–449.

Schaeffer, A., Lebedev, S. & Becker, T., 2016. Azimuthal seismic anisotropy in the earth's upper mantle and the thickness of tectonic plates, *J. geophys. Int.,* **207**(1), 901–933.

Stein, C. & Stein, S., 1992. A model for the global variation in oceanic depth and heat flow with lithospheric age, *Nature,* **359,** 123–129.

Sturgeon, W., Ferreira, A.M., Faccenda, M., Chang, S.-J. & Schardong, L., 2019. On the origin of radial anisotropy near subducted slabs in the midmantle, *Geochem. Geophys. Geosyst.,* **20**(11), 5105–5125.

Tasaka, M., Zimmerman, M.E. & Kohlstedt, D.L., 2017. Rheological weakening of olivine+ orthopyroxene aggregates due to phase mixing: 1. Mechanical behavior, *J. geophys. Res.: Solid Earth,* **122**(10), 7584–7596.

Tromp, J., Komatitsch, D. & Liu, Q., 2008. Spectral-element and adjoint methods in seismology, *Commun. Comput. Phys.,* **3**(1), 1–32.

Turcotte, D. & Schubert, G., 2014. *Geodynamics,* **160–228, 263–334,** 425–463.

van der Hilst, R.D. & Spakman, W., 1989. Importance of the reference model in linearized tomography and images of subduction below the Caribbean plate, *Geophys. Res. Lett.,* **16**(10), 1093–1096.

Van der Lee, S. & Nolet, G., 1997. Upper mantle s velocity structure of north america, *J. geophys. Res.: Solid Earth,* **102**(B10), 22815–22838.

Wang, Z. & Dahlen, F.A., 1995. Spherical-spline parameterization of three-dimensional earth models, *Geophys. Res. Lett.,* **22**(22), 3099–3102.

Warren, J.M., Hirth, G. & Kelemen, P.B., 2008. Evolution of olivine lattice preferred orientation during simple shear in the mantle, *Earth planet. Sci. Lett.,* **272**(3–4), 501–512.

Witek, M., Chang, S.-J., Lim, D., Ning, S. & Ning, J., 2021. Radial anisotropy in east asia from multimode surface wave tomography, *J. geophys. Res.: Solid Earth,* **126**(7), e2020JB021201. https://doi.org/10.1029/2020JB021201.

Witek, M., Lee, S., Chang, S. & van der Lee, S., 2023. Waveform inversion of large data sets for radially anisotropic earth structure, *J. geophys. Int.,* **232**(2), 1311–1339.

Woodhouse, J.H., 1988. *The Calculation of Eigenfrequencies and Eigenfunctions of the Free Oscillations of the Earth and the Sun,* pp. 321–370, Academic Press.

Yang, J. & Faccenda, M., 2020. Intraplate volcanism originating from upwelling hydrous mantle transition zone, *Nature,* **569,** 88–91.

Zhang, S. & Karato, S.-I., 1995. Lattice preferred orientation of olivine aggregates deformed in simple shear, *Nature,* **375**(6534), 774–777.